Phase stability and magnetic properties in fcc Fe-Cr-Mn-Ni alloys from first-principles modeling

Mark Fedorov [*]

Faculty of Materials Science and Engineering, Warsaw University of Technology, Wołoska 141, 02-507, Warsaw, Poland
and CCFE, United Kingdom Atomic Energy Authority, Abingdon OX14 3DB, United Kingdom

Jan S. Wróbel [†]

Faculty of Materials Science and Engineering, Warsaw University of Technology, Wołoska 141, 02-507, Warsaw, Poland

Antonio Fernández-Caballero [‡]

CCFE, United Kingdom Atomic Energy Authority, Abingdon OX14 3DB, United Kingdom
and EPSRC Centre for Doctoral Training in Materials for Demanding Environments, Faculty of Science and Engineering,
University of Manchester, Manchester M13 9PL, United Kingdom

Krzysztof J. Kurzydłowski

Faculty of Mechanical Engineering, Białystok University of Technology, Wiejska 45C, 15-351 Białystok, Poland

Duc Nguyen-Manh [§]

CCFE, United Kingdom Atomic Energy Authority, Abingdon OX14 3DB, United Kingdom

Systematic investigation of phase stability of the magnetic fcc Fe-Cr-Mn-Ni system—promising candidate structural materials to replace conventional austenitic steels—has been performed using a combination of spin-polarized density-functional theory, cluster expansion, and Monte Carlo simulations. The developed model was able to reproduce all known ground states (GSs) in the studied system and to predict new ones with strongly negative formation enthalpy—ternary $CrMnNi_2$ and quaternary $FeCr_2MnNi_4$. Investigation of phase stability was done at 0 K and finite temperatures in the whole concentration range and allowed us to observe the important role of Ni and Mn. Ni is the only element in the system that increases the order-disorder transition (ODT) temperature, which means that the fcc alloys with decreased concentration of Ni will form solid solutions at lower temperatures. Analysis of the effect of the addition of Mn to Fe-Cr-Ni alloy confirms a general trend of statistical correlation between the averaged magnitude of magnetic moments and volume per atom found from the predicted stable structures in the quaternary system and underlying subsystems. This linear magneto-volume relationship trend is, however, weaker in Fe-Cr-Mn-Ni alloys in comparison with those in the Fe-Cr-Ni system. Furthermore, Ni and Mn form the most stable GS—$L1_0$-MnNi, which has one of the strongest tendencies to segregate in fcc Fe-Cr-Mn-Ni alloys evidenced by the strength of Mn-Ni short-range ordering (SRO). Mn-Ni SRO significantly increases ODT temperature in the vicinity of $L1_0$-MnNi and to the equiatomic region. The ODT of $Cr_{18}Fe_{27}Mn_{27}Ni_{28}$ alloy is found to be 1290 ± 150 K, which supports the experimental observation of the disordered solid solution structure in $Cr_{18}Fe_{27}Mn_{27}Ni_{28}$ alloy at higher temperatures.

I. INTRODUCTION

High-entropy alloys (HEAs) are a relatively new group of materials, first described by Cantor *et al.* in Ref. [1], who studied the equiatomic CoCrFeMnNi alloy and reported its as-cast disordered single-phase fcc solid solutions with outstanding mechanical properties. Initially explained as being stabilized by high configurational entropy of mixing, HEAs have drawn attention to the central regions of the multicomponent phase diagrams and their industrial production and application [2]. HEAs are roughly described as alloys with the composition of 4 or more elements in equal or near-equal ratios of concentrations. However, the definition and the formation criteria are still not formally defined [3]. Yeh *et al.* [4,5] in 2004 described the empirical "four core effects" characteristic to HEAs, which include severe lattice distortion, slow diffusion rate, cocktail effect, and high configurational entropy. Since then, it has been shown that the aforementioned effects are not

---
[*]markfedorov93@gmail.com
[†]Corresponding author: jan.wrobel@pw.edu.pl
[‡]Currently affiliated with the Department of Engineering Science, University of Oxford, Parks Road, Oxford, OX1 3PJ, United Kingdom.
[§]Corresponding author: duc.nguyen@ukaea.uk

equally present in all HEAs [3], including the Cantor alloy [6], and as such need to be revisited.

Currently, many groups of HEAs are being studied, showing better properties than conventional materials in their groups. Examples [7] include: refractory HEAs (such as NbMoTaW), low-density HEAs (such as $Li_{20}Mg_{10}Al_{20}Sc_{20}Ti_{30}$), ceramic HEAs, and transition metal HEAs (such as the Cantor alloy).

In particular, HEAs have been shown to exhibit better resistance to irradiation damage compared to pure metals [8] and conventional austenitic steels [9–11]. This is attributed to their compositional complexity [10,11] and would make them good candidates for irradiation-facing materials in fusion and fission reactors. The main additional requirement is the absence of Co because it forms radioactive isotopes under irradiation. An alloy with the composition $Cr_{18}Fe_{27}Mn_{27}Ni_{28}$, investigated in the Oak Ridge National Laboratory (ORNL) both experimentally [9] and theoretically [12], has shown good radiation-resistance properties. Thus, the Fe-Cr-Mn-Ni system has been chosen for investigation in this paper. The $Cr_{18}Fe_{27}Mn_{27}Ni_{28}$ alloy has been reported to have fcc structure. Rough estimation of relative phase stability based on valence electron concentration (VEC), as it has been done in Refs. [13,14], indicates that the region with VEC higher than 8 shows the increased stability of fcc phase compared to bcc phase and accounts for ∼38% of the possible compositions in Fe-Cr-Mn-Ni system. Moreover, for a total of ∼85% of the structures VEC is higher than 7, in which fcc can coexist with bcc. Therefore, this paper is focused on the investigation of the fcc phase stability of the Fe-Cr-Mn-Ni system.

In order to explain the physical background of special behavior and understand the mechanisms of HEA formation in the Fe-Cr-Mn-Ni system, a vast range of concentrations has to be studied. Nowadays, theoretical methods of materials investigation on atomic scales are being intensively applied to study HEAs [15] since they are cheaper and more time-efficient than similar experimental investigations, and they make it possible to pin down the important compositions for further experimental studies. Usually, the theoretical methods are narrowed down to either a special quasirandom structure (SQS) approach or coherent potential approximation (CPA), which allow investigating only the disordered phases. Both of the methods have been used in a paper on defect properties of the $Cr_{18}Fe_{27}Mn_{27}Ni_{28}$ alloy that was approximated as the equiatomic FeCrMnNi alloy in a disordered state [12]. However, other experimental studies show that the single-phase disordered solid solution in the as-cast state (e.g., FeNiMnCr_{18} [16] and $Cr_{18}Fe_{27}Mn_{27}Ni_{28}$ [9]) does not always remain in this phase composition after annealing at temperatures below 973 K, which is within the working temperature range for irradiation-facing materials. Decomposition of single-phase disordered solid solution has been observed in $Fe_{40}Mn_{28}Ni_8Cr_{24}$ [17], CrMnFeCoNi [18–21] (Cr-rich bcc or σ phases), and CrMnFeCoNi [20] (B2-FeCo and $L1_0$-MnNi phases). Therefore, attention should be paid to the phase stability of HEAs at a broad range of temperatures, preferably from 0 K to the melting point.

A combination of methods that allows investigating the phase stability at such temperature range for the large amount of compositions, namely density-functional theory (DFT),

cluster expansion (CE), and Monte Carlo (MC), has been applied in Ref. [22] to study the finite-temperature phase stability of ternary Fe-Cr-Ni system in both bcc and fcc lattices and was successful at reproducing the experimental short-range order (SRO) parameters and ODT temperatures. DFT is one of the most commonly used methods in solid-state physics, which utilizes the dependency of total energy of quantum-mechanical ground state on electronic density [23–26]. DFT can be used to find the quantum-mechanical ground state and from there to study various properties on atomic scale [15,27], particularly the phase stability and magnetic properties at 0 K. The properties and phenomena at finite temperatures can be investigated by means of statistical mechanics simulations, and in order to that, it is first required to have knowledge of interactions in the system, the so-called effective cluster interactions (ECIs) [28]. These can be obtained via a generalized Ising Hamiltonian approach, which is usually implemented as structure inversion method (SIM) [29] within CE [30]. Another method that allows for statistical mechanics simulations is CPA-based general perturbation method (CPA-GPM) [31]. However, the perturbations are made in the vicinity of the fully disordered alloy. Since CPA-GPM utilizes a single-site approximation, it operates on the simple lattice of identical atoms with information only about the average occupancies on these lattice sites. Both CE-SIM and the extended CPA [32,33] make it possible to obtain temperature-dependent SRO parameters and from these to find the ODT temperatures, but, as it has been noted, the SRO fluctuations in CPA are restricted to disordered alloys representing a high-temperature state. On the other hand, the CE-based Monte Carlo simulations, which utilize many-body interactions, produce representative structures with distinct atomic positions at each chosen temperature and allow for observation of the decomposition of a fully disordered alloy into more stable phases from high to low temperatures. This fact is important for the investigation of alloys working in a broad temperature range. Hence, the cluster expansion method and Monte Carlo simulations will be used in this work.

To summarize, the combination of DFT, CE, and MC methods is used in this paper, serving both as a cross-check of Ref. [22] and an extension of the Fe-Cr-Ni into Fe-Cr-Mn-Ni. This was used to investigate the phase stability as a function of temperature and composition in the whole concentration range of fcc Fe-Cr-Mn-Ni, which is useful in designing alloys with the required atomic structure and properties for the applicable temperature range. This allowed for the study of temperature-dependent short-range order parameters and the generation of representative structures of alloys in the whole concentration range. In particular, it helped to understand the differences between the $Cr_{18}Fe_{27}Mn_{27}Ni_{28}$ alloy from Oak Ridge National Laboratory [9,12] and the equiatomic FeCrMnNi alloy. The representative structures will be used in the future for the investigation of defect properties of Fe-Cr-Mn-Ni alloys with realistic short-range order to explain their good irradiation resistance.

This paper is structured as follows. Computational methodology section (Sec. II) consists of cluster expansion formalism for multicomponent system (Sec. IIA), formalism for the calculation of chemical short-range order parameters (Sec. IIB), short discussion of the configurational entropy contribution
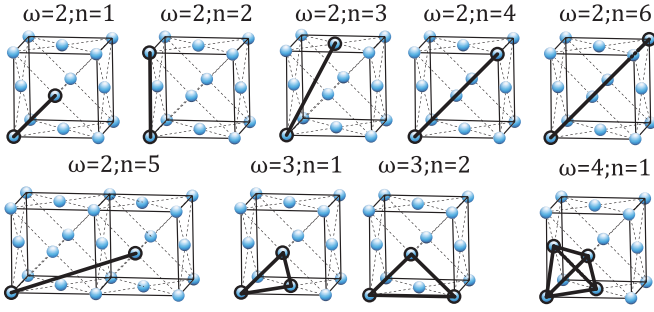
FIG. 1. Undecorated two-, three-, and four-body clusters with size ω and label n, which are used in this work.

(Sec. IIC), and the computational details for different methods used in the current work (Sec. IID). Phase stability at $T = 0$ K based on DFT calculations results is presented in Sec. III for Fe-Cr-Mn-Ni quaternary and its subsystems containing Mn (Secs. IIIA–IIID). The summary of cluster expansion application is described in Sec. IIIE. Finite temperature phase stability analysis is presented in Sec. IV which includes the results for a configurational entropy from a combined Monte Carlo and cluster expansion methods (Sec. IVA) and its contribution to the free energy of mixing (Sec. IVB), the order-disorder transition temperatures (Sec. IVC) and short-range order parameters (Sec. IVD) which have been studied in the whole concentration range. The main results of the current work are summarized in the Conclusions section.

II. COMPUTATIONAL METHODOLOGY

A. Cluster expansion formalism for multicomponent system

The enthalpy of mixing of an alloy with chosen configuration represented by a vector of configurational variables $\vec{\sigma}$ can be calculated from DFT using the value of total energy per atom of simulated alloy structure $E_{\text{tot}}^{\text{lat}}(\vec{\sigma})$ and the corresponding pure elements $E_{\text{tot}}^{\text{lat}}(p)$ underlying the same lattice as the alloy structure as follows:

$$H_{\text{mix}}(\vec{\sigma}) = E_{\text{tot}}^{\text{lat}}(\vec{\sigma}) - \sum_{p=1}^{K} c_p E_{\text{tot}}^{\text{lat}}(p), \tag{1}$$

where K is the number of alloy components and c_p are the average concentrations of each alloy component. Enthalpy of formation (H_{form}) is calculated as the energy of the structure with respect to the energies of pure element ground states (GSs).

In the cluster expansion formalism, the enthalpy of mixing can be parametrized as a polynomial in the occupational variables [34]:

$$H_{\text{mix}}(\vec{\sigma}) = \sum_{\omega,n,s} J_{\omega,n}^{(s)} m_{\omega,n}^{(s)} \langle \Gamma_{\omega',n'}^{(s')}(\vec{\sigma}) \rangle_{\omega,n,s}, \tag{2}$$

where the summation is performed over all the clusters, distinct under symmetry operations in the studied lattice, represented by the following parameters: ω and n are the cluster size (the number of lattice points in the cluster) and its label (the maximal distance between two atoms in the cluster in terms of coordination shells), respectively, see Fig. 1; (s) is the decoration of a cluster by point functions $\gamma_{j,K}(\sigma_i)$;

$m_{\omega,n}^{(s)}$ denotes the site multiplicity of the decorated clusters (in per-lattice-site units); and $J_{\omega,n}^{(s)}$ represents the ECI energy corresponding to the same (s) decorated cluster.

$\langle \Gamma_{\omega',n'}^{(s')}(\vec{\sigma}) \rangle_{\omega,n,s}$ are the cluster functions, averaged over all the clusters of size ω' and label n' decorated by the sequence of point functions (s') that are equivalent by symmetry to the cluster ω, n and decorated by the same sequence of point functions (s). Later in the text, $\langle \Gamma_{\omega',n'}^{(s')}(\vec{\sigma}) \rangle_{\omega,n,s}$ is referred to as $\langle \Gamma_{\omega,n}^{(s)}(\vec{\sigma}) \rangle$ for ease of notation. In Monte Carlo formalism, cluster functions are also averaged over all MC steps at chosen temperature, which has an effect on the accuracy and the computational costs of the calculations.

The cluster function $\Gamma_{\omega,n}^{(s)}(\vec{\sigma})$ is then defined as the product of orthonormal point functions of occupation variables [35] $\gamma_{j,K}(\sigma_i)$ for a specific cluster described by ω and n:

$$\Gamma_{\omega,n}^{(s)}(\vec{\sigma}) = \gamma_{j_1,K}(\sigma_1)\gamma_{j_2,K}(\sigma_2)\cdots\gamma_{j_\omega,K}(\sigma_\omega), \tag{3}$$

where the sequence $(s) = (j_1, j_2, \ldots, j_\omega)$ is the decoration of cluster by point functions, and the definition of point functions is the same as in Ref. [36]:

$$\gamma_{j,K}(\sigma_i) = \begin{cases} 1 & \text{if } j = 0, \\ -\cos\left(2\pi \lceil \frac{j}{2} \rceil \frac{\sigma_i}{K}\right) & \text{if } j > 0 \text{ and odd}, \\ -\sin\left(2\pi \lceil \frac{j}{2} \rceil \frac{\sigma_i}{K}\right) & \text{if } j > 0 \text{ and even}, \end{cases} \tag{4}$$

where $\sigma_i = i = 0, 1, 2, \ldots, (K-1)$, where numbers represent the constituent components of an alloy; j is the index of point functions $j = 0, 1, 2, \ldots, (K-1)$; and $\lceil \frac{j}{2} \rceil$ stands for the ceiling function–rounding up a number to the closest integer.

The matrix $\bar{\bar{\tau}}_K$, relating the point correlation functions to the point probabilities, can be constructed using point functions $\gamma_{j,K}(\sigma_i)$ as its elements:

$$(\bar{\bar{\tau}}_K) = \begin{bmatrix} \gamma_{j=0,K}(\sigma_i = 0) & \cdots & \gamma_{j=0,K}(\sigma_i = K-1) \\ \vdots & \ddots & \vdots \\ \gamma_{j=K-1,K}(\sigma_i = 0) & \cdots & \gamma_{j=K-1,K}(\sigma_i = K-1) \end{bmatrix}. \tag{5}$$

The exact $\bar{\bar{\tau}}_K$ matrices for two-, three-, and four-component systems are presented in Eq. (A1), Appendix A.

The general expression for the cluster correlation function is then may be determined using the $\bar{\bar{\tau}}_K$ matrix [35]:

$$\langle \Gamma_{\omega,n}^{(s)} \rangle = \sum_{A,B,\cdots} \left(\prod_\omega \bar{\bar{\tau}}_K \right)_{(s),A,B,\cdots} y_{\omega,n}^{AB\cdots}, \tag{6}$$

where $(\prod_\omega \bar{\bar{\tau}}_K)_{(s),A,B,\cdots}$ denotes the matrix direct product, i.e., the Kronecker product; the summation is done over the atomic species composing the alloy; $y_{\omega,n}^{AB\cdots}$ denotes the temperature-dependent *many*-body probability of finding atomic species $A, B, \cdots$ in the corresponding ω cluster with coordination shell, denoted by n.

Using the form of Eq. (6), two-body cluster correlation function is written in the following form [35]:

$$\langle \Gamma_{2,n}^{(s)} \rangle = \sum_{A,B} (\bar{\bar{\tau}}_K \otimes \bar{\bar{\tau}}_K)_{(s),A,B} y_{2,n}^{AB}, \tag{7}$$

where $\otimes$ denotes the matrix direct product. Three- and four-body correlation functions within the matrix formulation are

defined in a similar manner as Eq. (7) and are presented in Eq. (A2) and Eq. (A3).

The complete set of decorations (*s*) for a cluster of size ω corresponding to the K^ω list of indices is generated by applying the permutation representation of the space group # 225 (O_h^5) elements to the decorations belonging to the cluster and its subclusters. With symmetry, all correlation functions are generated from the given symmetrically unique set of correlations for each cluster in the Hamiltonian expansion.

B. Chemical short-range order parameters

Chemical SRO in the alloys can be analyzed using the Warren-Cowley SRO parameters. They can be obtained from the relation of pair probabilities and point probabilities by using the following expression:

$$\alpha_n^{AB} = 1 - \frac{y_{2,n}^{AB}}{c_A c_B}. \tag{8}$$

The Warren-Cowley SRO parameters have been formulated in Refs. [35,37] based on the principles, that, e.g., for clusters of two sites, the decorations indices can be interchanged because the space group O_h^5 contains twofold symmetry axes and translations that transform one site into the other. For clusters with more than two sites, the permutation operators are more complex and depend on the specific sites occupied in the clusters. For example, for the three-body cluster labeled by $\omega = 3; n = 2$ in Fig. 1, by using group theoretical arguments, it can be found that the symmetrically unique decoration (131) is equivalent to the (113), i.e., $\langle \Gamma_{3,2}^{(131)} \rangle \equiv \langle \Gamma_{3,2}^{(113)} \rangle$.

The fact that the inverse of a Kronecker product of two matrices is equivalent to the product of inverse matrices can be used to express the pair probabilities in terms of pair correlations. For this, the inverse of $\bar{\bar{\tau}}_K$ matrix, $\bar{\bar{\tau}}_K^{-1}$, can be obtained with its elements defined as follows [35]:

$$(\bar{\bar{\tau}}_K^{-1})_{ij} = \frac{1}{K} \begin{cases} 1 & \text{if } j = 0, \\ -2\sin\left(2\pi \lceil \frac{j}{2} \rceil \frac{\sigma_i}{K}\right) & \text{if } j > 0 \text{ and even}, \\ -2\cos\left(2\pi \lceil \frac{j}{2} \rceil \frac{\sigma_i}{K}\right) & \text{if } j > 0 \\ & \text{and } j < K - 1 \\ & \text{and } j \text{ is odd}, \\ -\cos\left(2\pi \lceil \frac{j}{2} \rceil \frac{\sigma_i}{K}\right) & \text{if } j = K - 1 \\ & \text{and } j \text{ is odd}. \end{cases} \tag{9}$$

The exact forms of $\bar{\bar{\tau}}_K^{-1}$ matrices for the two-, three-, and four-component systems in presented in Eq. (A4).

Using the $\bar{\bar{\tau}}_K^{-1}$ matrix, the point probability function is given by:

$$y_{1,1}^A = \sum_s (\bar{\bar{\tau}}_K^{-1})_{A,(s)} \langle \Gamma_{1,1}^{(s)} \rangle, \tag{10}$$

and from Eq. (7), the pair probability function is written as:

$$y_{2,n}^{AB} = \sum_s (\bar{\bar{\tau}}_K^{-1} \otimes \bar{\bar{\tau}}_K^{-1})_{A,B,(s)} \langle \Gamma_{2,n}^{(s)} \rangle. \tag{11}$$

The three- and four-body probability functions can be determined by the inverse of the respective cluster correlation functions and they are presented in Eqs. (A5) and (A6).

Since MC simulations with ECIs from CE give information about $\langle \Gamma_{2,n}^{(s)} \rangle$, the Warren-Cowley SRO parameters can be easily calculated directly from the MC simulations. They are determined in terms of correlation functions from MC simulations using the matrix formulation from Eq. (9). The explicit formula for the SRO Warren-Cowley parameter is expressed as:

$$\alpha_n^{AB} = 1 - \frac{\sum_s (\bar{\bar{\tau}}_K^{-1} \otimes \bar{\bar{\tau}}_K^{-1})_{A,B,(s)} \langle \Gamma_{2,n}^{(s)} \rangle}{\left[\sum_s (\bar{\bar{\tau}}_K^{-1})_{A,(s)} \langle \Gamma_{1,1}^{(s)} \rangle\right] \left[\sum_s (\bar{\bar{\tau}}_K^{-1})_{B,(s)} \langle \Gamma_{1,1}^{(s)} \rangle\right]}. \tag{12}$$

The exact formulas for the calculation of the Warren-Cowley SRO parameters for each pair of atoms in the four-component system, used in this work, are presented in Eq. (A7), which were formulated in Ref. [37].

C. Entropy contribution

Free energy of mixing for the alloy is defined as follows:

$$F_{\text{mix}}(T) = H_{\text{mix}}(T) - T S_{\text{mix}}(T), \tag{13}$$

where the mixing entropy term

$$S_{\text{mix}}(T) = S_{\text{mix}}^{\text{conf}}(T) + S_{\text{mix}}^{\text{vib}}(T) + S_{\text{mix}}^{\text{el}}(T) + S_{\text{mix}}^{\text{mag}}(T), \tag{14}$$

consists of configurational, vibrational, electronic, and magnetic mixing entropy contributions.

In this work, each contribution from Eq. (14) to the mixing entropy is defined as:

$$S_{\text{mix}}(T) = S_{\text{ideal}} - S_{\text{real}}(T), \tag{15}$$

where S_{ideal} is the entropy of the chosen structure in a fully disordered state, and $S_{\text{real}}(T)$ is the entropy of a structure with a configuration, obtained from the Monte Carlo simulations at a temperature T.

The maximum value of configurational entropy of a chosen alloy, meaning the value for the fully disordered structure, is defined as:

$$S_{\text{ideal}}^{\text{conf}}(T) = -k_B \sum_{p=1}^K c_p \ln(c_p), \tag{16}$$

where c_p is the concentration of the pth element in the alloy with the total number of elements equal to K. The maximum value for configurational entropy in a K-component system is possessed by the equiatomic alloy and can be calculated as $S_{\text{max}}^{\text{conf}}(T) = k_B \ln K$.

The cluster contribution to the entropy is determined from Monte Carlo calculations of correlation functions using the approach established in Ref. [35]. The generalized formula for the entropy, taking into account all *many*-body interactions, is then expressed as:

$$S_{\omega,n}^{\text{conf}} = k_B \sum_q w_q^{\omega,n} \sum_s y_q^{(s)} \ln\left(y_q^{(s)}\right), \tag{17}$$

where index (*s*) of the inner sum runs for all possible decorations of clusters of any given cluster indexed by q, which are given by K^{ω_q} total decorations. The weights in the sum are worked out following the iterative Barker formula [38] in the formalism of the cluster variation method. Detailed derivation

is formulated elsewhere [35], and the explicit values are listed in the Supplemental Material [39], Table SIII.

Other entropy contributions have been defined [40–43] and applied to HEAs in various works to calculate vibrational [44,45], electronic [12,46,47], and magnetic [45,46,48] contributions. It should be noted that the aforementioned papers utilize a variety of methods, including CPA, magnetic CE, and SQSs.

Relative magnitudes of the aforementioned contributions to the mixing entropy have been estimated in Refs. [3,5,44,45,49,50] as follows: $S_{\rm mix}^{\rm conf} > S_{\rm mix}^{\rm vib} > S_{\rm mix}^{\rm el} \approx S_{\rm mix}^{\rm mag}$. The maximal magnitude of $S^{\rm vib}$ can reach up to 6–12 times larger than the maximal value of $S^{\rm conf}$, which depends on the number of alloy components [44,45,48]. $S^{\rm vib}$ influences the total stability of the composition, but in order to find the relative stability of the ordered and disordered phases, the vibrational entropy of mixing (also called the excess entropy), $S_{\rm mix}^{\rm vib}$, should be considered.

The ratio of vibrational and configurational entropies of mixing also influences the order-disorder transition temperature [50]. The values of $S_{\rm mix}^{\rm vib}$ for two-component alloys have been shown in Ref. [50] to reach a maximum of $0.2k_B$ (compared to the maximum of $S_{\rm mix}^{\rm conf} = 0.693k_B$), meaning the ∼30% correction to the order-disorder transition temperature. In the four-component MoTaNbW HEA, the change of vibrational entropy between ordered and disordered phases is negligible, especially compared to 50% change (∼$0.7k_B$) in the configurational entropy [44] between those two considered phases, which depends purely on the level of ordering in the system. Hence, even though the vibrational, electronic and magnetic mixing entropies influence the stability of the alloy, the main entropic contribution to $F_{\rm mix}$ comes from configurational mixing entropy. As such, only the effect of configurational mixing entropy will be investigated in the current work.

D. Computational details

DFT calculations with collinear spin-polarization were performed using the projector augmented wave (PAW) method implemented in VASP [51–56]. Exchange and correlation were treated in the generalized gradient approximation GGA-PBE [57]. The core configurations of Fe, Cr, Mn, and Ni in PAW potentials were $[\rm Ar]3d^74s^1$, $[\rm Ar]3d^54s^1$, $[\rm Ar]3d^64s^1$, and $[\rm Ar]3d^94s^1$, respectively.

Total energies were calculated using Γ-centered Monkhorst-Pack mesh [58] of k-points in the Brillouin zone, with the k-mesh spacing of 0.02 Å^{-1}. This corresponds to $12 \times 12 \times 12$ k-point mesh for a four-atom fcc conventional unit cell. The plane wave cutoff energy used in the calculations was 400 eV. Cutoff energy and k-mesh spacing have been chosen the same as in Ref. [22]. The total energy convergence criterion was set to 10^{-6} eV/cell, and force components were relaxed to 10^{-4} eV/Å.

The basic idea of SQSs is to generate a minimally sized supercell that approximates a random (disordered) solid solution. Therefore both energies and structural properties calculated from SQSs can be used to compare with those predicted for ordered or partially ordered alloy configurations obtained within the CE method. SQSs have been generated using the method based on a Monte Carlo–simulated annealing loop with an objective function that seeks to perfectly match the maximum number of correlation functions, implemented in the `mcsqs` code of the ATAT package [59]. SQSs have been produced for binary structures with the 12.5 at. % concentration step in 32-atom supercells, and later calculated with DFT using the aforementioned parameters for all considered binary systems.

Mapping of DFT energies to CE energies for ordered structures was performed using the ATAT package [34,36,60,61]. SQSs have not been included in the mapping. In order to find ECIs for binary fcc alloys, the initial database of 28 structures from Ref. [62] was used. For ternary fcc alloys, the initial database consisted of 98 structures adapted from Ref. [63]. The quaternary database was constructed following the approach from Ref. [22]: the ternary database was considered, the symmetry and the number of nonequivalent positions (NEPs) in each structure was checked and the structures with the number of NEPs greater than three were included in the quaternary fcc structure database by populating the higher NEPs with various combinations of elements.

Ordered Fe-Cr-Mn-Ni alloys show complex magnetic behavior even in collinear calculations with competing stability of nonmagnetic (NM), ferromagnetic (FM), layered antiferromagnetic (AFM), and ferrimagnetic (FiM) configurations. Thus, full relaxations starting from various initial magnetic configurations were performed for ordered structures, used in the construction of the CE model, in order to find the most stable magnetic configuration characterizing a given structure. Initial magnitudes of magnetic moments have been set to $2.2\mu_B$ for Fe, $1.5\mu_B$ for Cr, $2.5\mu_B$ for Mn, and $0.7\mu_B$ for Ni. Magnetic structure of binary SQSs without Cr has been initialized as FM, and in SQSs with Cr, the magnetic moment of Cr has been initialized as oriented anti-parallel to the magnetic moments of other compounds.

Only the most stable magnetic configurations for each composition have been taken into account during the construction of the data set, which later has been mapped to CE, which was used to account for the magnetism in an implicit way. The CE routine of the ATAT code has produced a number of structures, absent in the initial data set. This helped to construct a more precise concentration mesh of structures, calculated with DFT. Fitting of the final DFT structures data set to CE produced the ECIs, which were used in the following MC simulations.

The predictive accuracy of the CE model is usually quantitatively estimated via the cross-validation score (CVS):

$$\mathrm{CVS}^2 = \frac{1}{N} \sum_{i=1}^{N} \left[E_{\rm DFT}^i - E_{\rm CE'}^{(i)} \right]^2, \qquad (18)$$

where $E_{\rm CE'}^{(i)}$ is the energy of the ith structure, predicted by fitting CE energies to DFT energies, excluding $E_{\rm DFT}^i$ of the ith structure. As such, the errors from DFT calculations will inevitably propagate into the CE model. Since CE predicts the energy of the ith structure by fitting the existing DFT data, the initial set of structures can yield a different $E_{\rm CE'}^{(i)}$ and, as a result, different ECIs. A particular case of the different sets of structures is the difference in the concentration meshes. Both aforementioned problems, nevertheless, should

be counteracted by the construction of a uniformly spaced and sufficiently large data set.

Mapping of the mixing enthalpies of 835 structures was conducted for the quaternary system and the cross-validation score of 13 meV was achieved. Such value of CVS is considered to be reasonable taking into account the complex magnetic structure of the investigated system. Various sets of clusters have been tested, starting from 1 smallest two-body cluster up to the cluster set with 8 two-body, 7 three-body, and 3 four-body clusters, following the rules from Ref. [64]. Although the cluster sets for all subsystems are not required to be the same, the cluster set for the system with more elements should adequately describe the underlying subsystems with fewer elements. The clusters set for the quaternary system should be applicable for all the underlying ternary and binary subsystems. The set of clusters that have minimized CVS for the quaternary system consists of 6 two-body, 2 three-body, and 1 four-body undecorated clusters, illustrated in Fig. 1. And since this set of clusters reasonably describes the underlying systems with difference smaller than 1 meV between the chosen set and the best set for each system, it has been chosen as uniform for all underlying subsystems.

Therefore, the enthalpy of mixing for all considered systems in the CE formalism can be written as:

$$
\begin{aligned}
H_{\text{mix}}(\vec{\sigma}) &= \sum_{\omega,n,s} J_{\omega,n}^{(s)} m_{\omega,n}^{(s)} \langle \Gamma_{\omega,n}^{(s)}(\vec{\sigma}) \rangle \\
&= J_{1,1}^{(0)} \langle \Gamma_{1,1}^{(0)} \rangle + \sum_{s} J_{1,1}^{(s)} \langle \Gamma_{1,1}^{(s)} \rangle + \sum_{n=1}^{6} \sum_{s} m_{2,n}^{(s)} J_{2,n}^{(s)} \langle \Gamma_{2,n}^{(s)} \rangle \\
&\quad + \sum_{n=1}^{2} \sum_{s} m_{3,n}^{(s)} J_{3,n}^{(s)} \langle \Gamma_{3,n}^{(s)} \rangle + \sum_{s} m_{4,1}^{(s)} J_{4,1}^{(s)} \langle \Gamma_{4,1}^{(s)} \rangle,
\end{aligned}
$$

(19)

where $J_{\omega,n}^{(s)}$ are different in each studied subsystem.

Size ω, label n, decoration (s), multiplicity $m_{\omega,n}^{(s)}$, coordinates of points, and $J_{\omega,n}^{(s)}$ (in meV) of the aforementioned clusters for the fcc Fe-Cr-Mn-Ni system and all underlying subsystems are listed in Table I.

ECIs, obtained using the structure inversion method [29], for studied binary and ternary subsystems as well as for the quaternary system are presented in the corresponding sections.

Semicanonical MC simulations were performed also using the ATAT package. Most of the simulations were performed using a cell containing 2048 atoms in the form of $8 \times 8 \times 8$ fcc unit cell. For each composition, simulations were performed starting from a disordered high-temperature state at $T = 3000$ K. The alloy was then cooled down with the temperature step of $\Delta T = 100$ K, with 2000 equilibration and accumulation Monte Carlo passes. TDI calculation for the equiatomic quaternary composition was performed with the temperature step of $\Delta T = 5$ K in order to obtain the accurate values of the configurational entropy.

III. PHASE STABILITY AT 0 K

A. Pure elements

Extensive calculations of total energy as a function of volume have been conducted for known and hypothetical crystal structures and magnetic configurations of Fe, Cr, Mn, and Ni in order to understand the stability of pure elements and obtain the reference energies of the most stable magnetic configurations for the CE method. A list of all considered structures is presented in Supplemental Material [39], Table SI.

The most stable fcc structures of pure elements from the current studies at 0 K are as follows: antiferromagnetic double layer (AFMDL) Fe, nonmagnetic (NM) Cr, ferromagnetic (FM) Ni, and antiferromagnetic single layer (AFMSL) Mn. True GSs of pure elements from the current studies at 0 K are the following: FM bcc Fe, AFM bcc Cr, FM fcc Ni, and AFM σ-phase α-Mn.

Experimental GSs of pure elements at 0 K are as follows: noncollinear FM bcc Fe [65], spin-density wave bcc Cr [66], and FM fcc Ni [65]. Experimental results for Mn indicate both collinear and noncollinear AFM σ-phase α-Mn [67–72]. However, the total energies per atom of collinear and noncollinear configurations obtained from DFT calculations [73] are almost indistinguishable. Analysis of the stability and magnetic moments of Mn and comparison to previous theoretical and experimental results are presented in Appendix B.

Due to the high calculation costs, noncollinearity has not been considered in the current work, and the enthalpies of formation have been calculated with respect to the collinear GSs.

Since the ground-state crystal lattices of Fe, Cr, Mn, and Ni belong to different crystallographic groups, the analysis of alloy stability in Secs. IIIB–IIID have been performed both in terms of enthalpy of mixing and enthalpy of formation. Since GS of Ni is fcc, it will act as a fcc phase stabilizer—the increase of Ni content will more likely result in the stabilization of fcc lattice structure. Contrary to Ni, Cr has the highest difference of $E_{\text{fcc}} - E_{\text{GS}} = 0.394$ eV, and therefore can inhibit a formation of fcc phase in favor of bcc phase. The values of $E_{\text{fcc}} - E_{\text{GS}}$ for Fe and Mn are 5 times smaller compared to Cr. These results are consistent with the empirical VEC estimation.

B. Binary subsystems

In this subsection, there are presented enthalpies of formation, enthalpies of mixing, volumes per atom and AMMMs obtained using DFT at 0 K for the binary systems containing Mn, namely Cr-Mn, Fe-Mn and Mn-Ni. Since the methodology and the results for Fe-Cr, Cr-Ni and Fe-Ni are similar to ones used and obtained in Ref. [22], they are described in Appendix C. For each binary system, the results obtained for the ordered structures are compared to the results obtained for the SQSs.

In the plots within this subsection, formation energies of the most stable pure fcc structures are connected by a dashed line that represents the "zero line" of mixing enthalpies of the considered systems, so all structures with energies below

TABLE I. Size ω, label n, decoration (s), coordinates of points in the relevant clusters on fcc lattice, multiplicity $m_{\omega,n}^{(s)}$, and $J_{\omega,n}^{(s)}$ (in eV/atom) for the fcc Fe-Cr-Mn-Ni system and all underlying binary and ternary subsystems. Index (s) is the same as the sequence of points in the relevant cluster.

ω	n	(s)	Coordinates	$m_{\omega,n}^{(s)}$	$J_{\omega,n}^{(s)}$										
					CrFe	CrMn	CrNi	FeMn	FeNi	MnNi	CrFeMn	CrFeNi	CrMnNi	FeMnNi	FeCrMnNi
1	1	(0)	(1,1,1)	1	−0.063	−0.011	−0.114	0.014	−0.058	−0.011	−0.026	−0.085	−0.055	0.012	−0.041
		(1)		1	−0.026	0.014	0.031	−0.011	−0.049	−0.083	0.061	0.036	0.070	−0.001	0.113
		(2)		1							0.039	−0.042	0.113	0.098	−0.041
		(3)		1											−0.009
2	1	(1,1)	(1,1,1)	6	0.010	0.001	0.013	0.009	0.010	0.023	0.008	0.012	0.023	0.001	0.009
		(2,1)	(1,3/2,3/2))	12							−0.007	0.001	0.001	0.001	0.000
		(3,1)		12											0.003
		(2,2)		6							0.010	0.007	0.007	0.004	0.000
		(3,2)		12											0.001
		(3,3)		6											0.006
2	2	(1,1)	((1,1,1),	3	−0.006	−0.001	−0.011	−0.019	−0.003	−0.032	−0.009	−0.028	−0.027	−0.021	−0.009
		(2,1)	(1,1,0))	6							0.004	−0.003	0.005	0.004	0.000
		(3,1)		6											−0.004
		(2,2)		3							−0.008	−0.005	−0.008	−0.033	−0.012
		(3,2)		6											−0.004
		(3,3)		3											−0.009
2	3	(1,1)	((1,1,1),	12	0.003	0.002	0.007	−0.002	0.002	−0.007	0.005	0.007	0.001	0.003	0.001
		(2,1)	(2,3/2,3/2))	24							−0.001	0.002	−0.008	−0.002	0.003
		(3,1)		24											0.004
		(2,2)		12							−0.001	0.002	0.002	−0.009	0.002
		(3,2)		24											0.000
		(3,3)		12											0.000
2	4	(1,1)	((1,1,1),	6	0.000	0.002	0.001	−0.001	0.001	−0.002	0.001	0.001	−0.002	0.000	0.000
		(2,1)	(2,1,2))	12							0.001	0.002	−0.004	−0.002	0.002
		(3,1)		12											0.001
		(2,2)		6							−0.003	0.001	0.000	−0.002	0.001
		(3,2)		12											0.001
		(3,3)		6											−0.001
2	5	(1,1)	((1,1,1),	12	−0.001	−0.001	−0.003	−0.001	0.000	0.006	−0.002	−0.003	0.002	−0.003	−0.001
		(2,1)	(1,3/2,−1/2))	24							0.000	−0.001	0.006	0.000	−0.003
		(3,1)		24											−0.002
		(2,2)		12							−0.001	0.000	−0.001	0.008	0.000
		(3,2)		24											0.001
		(3,3)		12											0.000
2	6	(1,1)	((1,1,1),	4	0.000	0.000	−0.001	0.004	−0.002	−0.002	0.001	0.001	−0.004	0.002	0.001
		(2,1)	(2,2,0))	8							−0.001	0.000	−0.003	0.005	0.002
		(3,1)		8											0.001
		(2,2)		4							0.002	−0.003	0.000	−0.002	−0.003
		(3,2)		8											−0.001
		(3,3)		4											0.000
3	1	(1,1,1)	((1,1,1),	8	−0.001	−0.001	0.002	−0.003	0.005	0.007	0.000	0.007	−0.008	−0.007	0.000
		(2,1,1)	(3/2,1,1/2),	24							−0.001	−0.003	−0.003	−0.003	0.001
		(3,1,1)	(1,3/2,1/2))	24											0.002
		(2,2,1)		24							0.001	0.002	−0.002	0.006	−0.003
		(3,2,1)		48											0.000
		(3,3,1)		24											0.001
		(2,2,2)		8							−0.004	0.003	0.000	−0.003	0.000
		(3,2,2)		24											0.002
		(3,3,2)		24											−0.001
		(3,3,3)		8											0.000

TABLE I. (*Continued.*)

ω	n	(s)	Coordinates	$m_{\omega,n}^{(s)}$	$J_{\omega,n}^{(s)}$										
					CrFe	CrMn	CrNi	FeMn	FeNi	MnNi	CrFeMn	CrFeNi	CrMnNi	FeMnNi	FeCrMnNi
3	2	(1,1,1)	((1,1,1),	12	0.002	−0.001	−0.004	0.002	0.000	0.003	−0.003	−0.008	0.001	−0.001	−0.001
		(2,1,1)	(1,3/2,1/2),	24							0.001	0.000	0.000	0.005	0.001
		(3,1,1)	(1,1,0))	24											0.001
		(1,2,1)		12							0.000	−0.001	−0.012	−0.006	−0.002
		(2,2,1)		24							0.000	0.002	−0.001	0.005	0.002
		(3,2,1)		24											−0.001
		(1,3,1)		12											−0.002
		(2,3,1)		24											0.000
		(3,3,1)		24											−0.001
		(2,1,2)		12							−0.006	0.000	0.004	−0.005	−0.006
		(3,1,2)		24											−0.001
		(2,2,2)		12							0.002	−0.001	−0.001	−0.006	−0.001
		(3,2,2)		24											0.000
		(2,3,2)		12											0.002
		(3,3,2)		24											0.001
		(3,1,3)		12											−0.002
		(3,2,3)		12											0.000
		(3,3,3)		12											−0.001
4	1	(1,1,1,1)	((1,1,1),	2	−0.003	−0.002	0.008	0.003	−0.001	−0.008	−0.005	0.015	−0.003	−0.008	−0.003
		(2,1,1,1)	(3/2,3/2,1),	8							−0.001	0.003	−0.010	0.006	0.002
		(3,1,1,1)	(3/2,1,1/2),	8											0.001
		(2,2,1,1)	(1,3/2,1/2))	12							−0.001	−0.003	0.001	0.005	−0.003
		(3,2,1,1)		24											0.001
		(3,3,1,1)		12											0.001
		(2,2,2,1)		8							0.000	0.010	−0.003	−0.012	−0.001
		(3,2,2,1)		24											−0.001
		(3,3,2,1)		24											0.001
		(3,3,3,1)		8											0.003
		(2,2,2,2)		2							0.002	−0.001	−0.007	−0.013	−0.001
		(3,2,2,2)		8											0.005
		(3,3,2,2)		12											0.001
		(3,3,3,2)		8											−0.002
		(3,3,3,3)		2											−0.002

and above this line possess negative and positive enthalpies of mixing, respectively. For the systems with compositions that have negative formation enthalpy (H_{form}), the "zero line" of formation enthalpy connecting the true GSs of considered systems is represented by a dash-dotted line. Convex hulls are indicated with respect to the most stable pure fcc structures, since the majority of the calculated compositions have positive H_{form} and the structures from fcc convex hull are treated as GSs in the cluster expansion model.

The effect of magnetism on the volume of structures is analyzed by comparing the calculated values of volume to the linear heuristic estimate, called the Vegard's law, in which the value of volume per atom for the alloy is equal to the sum of volumes per atom of it's constituents factoring their concentration.

1. Cr-Mn binary

Ground states of Cr-Mn system in terms of mixing enthalpy are Cr_3Mn [Z1(100)] and CrMn [Z2(100)], but all fcc Cr-Mn structures exhibit positive enthalpy of formation [see Fig. 2(a)], which is consistent with a fact that no stable fcc

phases are observed experimentally for this system. Enthalpy of mixing shows a tendency to decrease in the near-equiatomic concentration region, whereas enthalpy of formation shows a strong linear drop with the increase of Mn concentration. Formation enthalpies of SQSs are higher than the ones of ordered structures and their values converge to the values of NM Cr and NM Mn at the corresponding ends of the concentration scale.

Chromium suppresses high magnetic moment of Mn resulting in NM region with the Cr concentration larger than 50 at. %, where the volumes per atom follow almost perfectly Vegard's law for NM reference structures [see Fig. 2(b)]. For Cr concentration smaller than 50 at. %, the structures are FiM and the volumes per atom lie between magnetic and NM Vegard's law estimates, where Mn dominates the magnetic structure. Volumes of SQSs repeat the Vegard's law estimate for NM reference structures, although the magnetic ordering of SQSs with 25–50 at. % Cr is FiM. The value of AMMM increases with the increase of Mn concentration [see Fig. 2(c)]. The Cr-rich NM stability region and the Mn-rich FiM stability region are divided with NM CrMn structure.
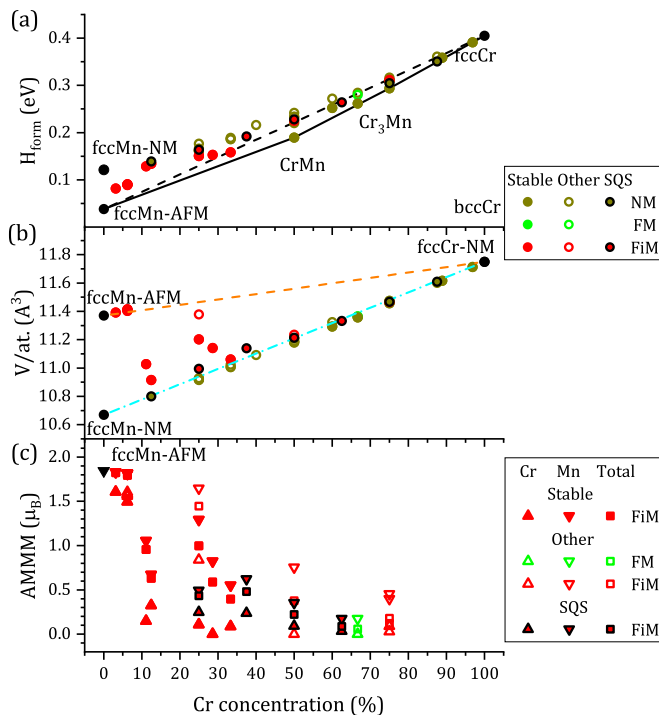
FIG. 2. (a) Enthalpy of formation, (b) volume per atom, and (c) average magnitudes of magnetic moments per atom of fcc Cr-Mn ordered and SQS structures calculated using DFT. Black solid line marks the convex hull of fcc structures. Black dashed line connects the most stable fcc structures of respective pure elements. Vegard's law estimate for magnetic and nonmagnetic fcc structures is indicated by the orange dashed line and blue dash-dotted line, respectively. The results obtained for the most stable structures and magnetic configurations for each considered alloy composition are indicated by filled markers, and the less stable structures are indicated by open markers. Values for SQS structures are indicated by filled markers with black edges.

2. Fe-Mn binary

The most stable GS of Fe-Mn binary in terms of enthalpy of mixing is L1$_2$-Fe$_3$Mn. The other GSs in terms of enthalpy of mixing are FeMn$_{31}$, FeMn$_{15}$, and Fe$_3$Mn$_4$. Trends in enthalpy of mixing [see Fig. 3(a)] are consistent with previous calculations [74]. The enthalpies of formation of all Fe-Mn structures are positive, which means that at 0 K there are no stable compositions from the point of view of enthalpy of formation. However the values of enthalpies tend to decrease in near-equiatomic concentration region, which is consistent with previous calculations [75] and with previous assessments of metastability of fcc alloys [76]. This can be related to the fact that the most stable α-Mn structure has much more complex lattice in GS compared to fcc, and GS of Fe is FM bcc within collinear calculations, although it should be noted that Fe has stable fcc lattice above 1190 K, and austenite steels, which have fcc lattice, can be stablized to exist even at room temperature. The study of Fe-Mn alloy powders has shown a presence of martensite (bcc) and austenite (fcc) [77,78]. The latter is observed as a single phase in Fe$_{70}$Mn$_{30}$ alloy [79], which is close in a concentration to the fcc Fe$_3$Mn GS.
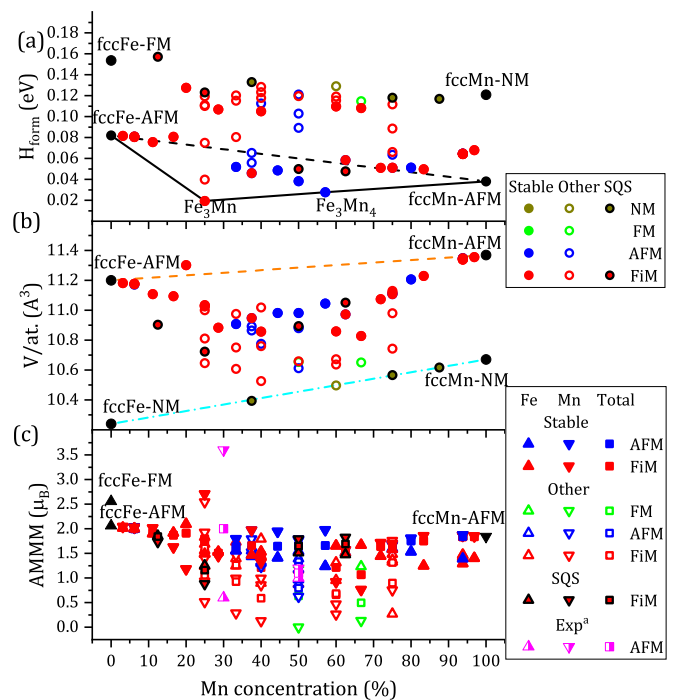

FIG. 3. (a) Enthalpy of formation, (b) average magnitudes of magnetic moments per atom, (c) volume per atom of fcc Fe-Mn structures calculated using DFT. The notation is the same as in Fig. 2. Experimental data (superscript a) are adapted from the work of Kubitz and Hayes [83].

SQSs are less stable than the ordered structures and the values of enthalpies of formation converge to the values of FM Fe and NM Mn at the corresponding ends of the concentration scale, but at 50 at. % Mn and 62.5 at. % Mn the values of H_{form} are much lower compared to other SQSs. The composition of these two structures is close to the AFM Fe$_3$Mn$_4$ ordered structure, which can explain such stability by a higher level of magnetic ordering.

In the Fe-Mn binary subsystem, the volumes of structures lie between the Vegard's law estimates for magnetic and nonmagnetic reference structures [see Fig. 3(b)]. Fe-rich and Mn-rich structures almost perfectly satisfy the estimate for magnetic reference structures, but tend to decrease with the proximity of Fe-Mn ratio to the equiatomic composition.

The antiferromagnetism in fcc Fe-Mn alloys was experimentally observed in wide range of concentrations [80–82]. Current results show that the magnetic moments of Mn atoms are antiferromagnetic to Fe for almost all structures. AMMMs of both elements slowly decrease with increasing Mn concentration [see Fig. 3(c)]. AMMM for fcc Fe$_{50}$Mn$_{50}$ structure is 1.5 μ_B, which is close to the experimental value of 1.2 μ_B estimated for Fe$_{50}$Mn$_{50}$ disordered solid solution in Ref. [81]. AMMMs of the system decrease slightly in the near-equiatomic region, consistent with the similar behavior of volume per atom. AMMMs are dominated by Fe atoms in the Fe-rich region and by Mn atoms in the Mn-rich region. AMMM of Mn atoms vary between the value for fcc AFMSL Mn in Mn-rich region and site-I magnetic moment from α-Mn in Fe-rich region (see Table V in Appendix B).
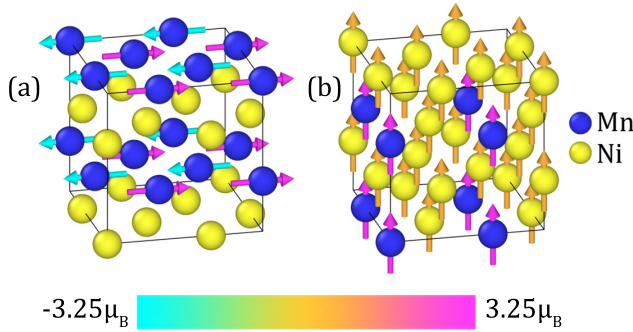
FIG. 4. Atomic structure and magnetic moments of the binary Mn-Ni GSs calculated in a conventional fcc $2 \times 2 \times 2$ super cell using collinear magnetism in DFT: (a) AFM $L1_0$-MnNi and (b) FM $L1_2$-MnNi$_3$. The color code of the arrows shows the magnitudes of magnetic moments.

3. Mn-Ni binary

Accoding to the current studies, the fcc Mn-Ni binary system has two GS in terms of both formation and mixing enthalpies [see Fig. 5(a)]: AFM $L1_0$-MnNi [see Fig. 4(a)] and FM $L1_2$-MnNi$_3$ at 75 at. % Ni [see Fig. 4(b)]. Both GSs have been observed experimentally [84–86]. The formation
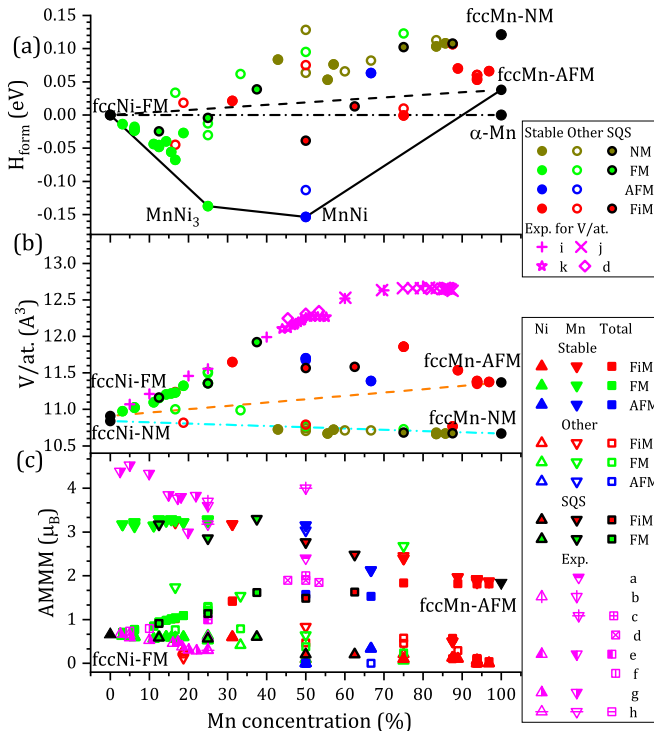

FIG. 5. (a) Enthalpy of formation, (b) average magnitudes of magnetic moments per atom, (c) volume per atom of fcc Mn-Ni structures calculated using DFT. The notation is the same as in Fig. 2. Black dash-dotted line connects the true GSs, which are FM fcc Ni and AFM α-Mn. Experimental data are as follows: [a] from Ref. [96], [b] from Ref. [91], [c] from Ref. [95], [d] from Ref. [90], [e] from Ref. [92], [f] from Ref. [98], [g] from Ref. [94], [h] from Ref. [93], [i] from Ref. [87], [j] from Ref. [88], [k] from Ref. [89].

enthalpy of $L1_0$-MnNi is the most negative among all studied structures, including ternary and quaternary (see Table II).

SQSs are less stable than the ordered structures and their formation enthalpies converge to the values of FM Ni and NM Mn at the corresponding ends of the concentration scale, but, similarly to FeMn binary, at 50 at. % Mn and 62.5 at. % Mn the values of H_{form} are much lower compared to the other SQSs. The composition of these two structures is close to the AFM $L1_0$-MnNi ordered structure, which can explain such stability by a higher level of magnetic ordering.

Volumes per atom for NM structures are in a good correspondence with the Vegard's law estimate for NM structures [see Fig. 5(b)]. On the other hand, the values of volumes per atom for both FM and FiM structures become highly overestimated, when moving from pure elements to the equiatomic concentration, compared to the Vegard's law estimate for magnetic structures. However, values of volumes per atom for the structures with Mn concentration between 0 and 30 at. %, which are mostly FM, are in an excellent correspondence with the experimental data from Refs. [87,88]. For higher Mn concentration the agreement gradually becomes worse, compared to experimental data from Refs. [89,90]. Volumes of FM SQSs in the Ni-rich end also closely correspond to the experimental data from Refs. [87,88] and this correspondence is observed in the wider range of concentrations, compared to the ordered structures—to 37.5 at. % Mn. This can suggest that the samples, studied in Ref. [87] had disordered FM structure, stabilized during the sample preparation.

Regions of stability of different magnetic configurations are divided by AFM $L1_0$-MnNi. Magnetic ordering of the most stable sturctures with more than 50 at. % Mn concentration is AFM or FiM [see Fig. 5(c)], and at Mn concentrations lower than 25 at. % the magnetic ordering of the most stable structures is FM, which is consistent with the experimental observations [91–93]. The boundary of this division is approximately 33 at. % Mn. The value of AMMM of Mn grows with the increasing Ni concentration, being equal to the value of magnetic moment for fcc AFMSL Mn (see Table V) at concentrations close to 0 at. % Ni, and equal to the value of magnetic moment of Type I atom in AFM α-Mn at concentrations close to 100 at. % Ni (see Table V). The values of AMMM are underestimated compared to the experimental results from Ref. [94] up to 20 at. % Mn, but are close at higher Mn concentration. The values of AMMM increase with the increase of Mn concentration. AMMM of Ni is very close to the experimental values from Ref. [94].

From current studies, Mn atoms in $L1_0$-MnNi form two sublattices, which are antiferromagnetically ordered to each other, with the Mn AMMM of 3.15 μ_B. Ni atoms do not have magnetic moments, which closely corresponds to one of the estimates in Ref. [95]. AMMM for Mn lies between the estimates from Refs. [95], 4 μ_B, and Ref. [96], 2.4 μ_B. Simulation and experimental results from Ref. [97] show that both bulk and thin film Mn$_{50}$Ni$_{50}$ have Mn in high-spin state with values of magnetic moment per atom of 2.8–3.9 μ_B and Ni with strongly reduced values of magnetic moment per atom. Total AMMM of 1.58μ_B is very close to the values from Ref. [90], 1.9 μ_B and adapted from Ref. [95], 2 μ_B.

In the fcc $L1_2$-MnNi$_3$ FM structure, Mn atoms have a magnetic moment of 3.25 μ_B, and Ni atoms have on average

TABLE II. Chemical composition, lattice symmetry with Wyckoff position (WP), magnetic symmetry with WP, magnetic moment on each magnetic WP (in μ_B), AMMM (in μ_B), magnetic ordering, volume per atom (in Å^3), and the formation enthalpy per atom of the most stable intermetallic phases with negative H_{form} (in eV) in fcc quaternary Fe-Cr-Mn-Ni system. The results from the present work are compared with the available experimental data.

Composition	Symmetry, WP	Mag. symm., WP	MM$_{\text{WP}}$, (μ_B)	AMMM, (μ_B) Current	Exp.	Magnetic ordering	Vol./at. (Å^3) Current	Exp.	H_{form} (eV)
CrNi$_2$	*Immm*	—		0		NM	10.92	11.36[a]	−0.018
	Cr$_1$ 2 a	Cr$_1$ 2 a	0						
	Ni$_1$ 4 e	Ni$_1$ 4 e	0						
CrNi$_8$	*I4/mmm*	*C2′/m′*		0.28	0.16[b]	FiM	10.89		−0.007
	Cr$_1$ 2 a	Cr$_1$ 2 a	−0.687						
	Ni$_1$ 8 h	Ni$_1$ 4 g	0.199						
	Ni$_2$ 8 i	Ni$_2$ 8 j	0.278						
		Ni$_3$ 4 i	0.178						
Fe$_3$Ni$_2$	*I4/mmm*	*C2′/m′*		1.81		FM	11.42	11.56[c]	−0.043
	Fe$_1$ 4 e	Fe$_1$ 4 i	2.591						
	Fe$_2$ 2 b	Fe$_2$ 2 d	2.652						
	Ni$_1$ 4 e	Ni$_1$ 4 i	0.607						
FeNi	*P4/mmm*	*Cmm′m′*		1.65	1.64[d], 1.52[e]	FM	11.33	11.53[f]	−0.069
	Fe$_1$ 1 d	Fe$_1$ 2 c	2.661						
	Ni$_1$ 1 a	Ni$_1$ 2 a	0.631						
FeNi$_3$	*Pm-3m*	*Pm′m′m*		1.2	1.21[d], 1.12[e]	FM	11.14	11.21[f,a]11.23[g]	−0.092
	Fe$_1$ 1 a	Fe$_1$ 1 a	2.914						
	Ni$_1$ 3 c	Ni$_1$ 1 f	0.631						
		Ni$_2$ 1 d	0.588						
		Ni$_3$ 1 g	0.673						
FeNi$_8$	*I4/mmm*	*P-1*		0.86	0.85[e]	FM	10.99	10.98[c]	−0.053
	Fe$_1$ 2 a	Fe$_1$ 1 a	2.814						
	Ni$_1$ 8 i	Ni$_1$ 2 i	0.643						
	Ni$_2$ 8 h	Ni$_2$ 2 i	0.599						
		Ni$_3$ 2 i	0.604						
		Ni$_4$ 2 i	0.604						
MnNi	*P4/mmm*	*P_Bmna*		1.58	1.9[h], 2.0[i]	AFM	11.7	12.27[j,k], 12.31[h]	−0.154
	Mn$_1$ 1 d	Mn$_1$ 2 d	3.151						
	Ni$_1$ 1 a	Ni$_1$ 2 b	0						
MnNi$_3$	*Pm-3m*	*Pm′m′m*		1.21	1.1[l], 1.02[d]	FM	11.36	11.56[g,a]	−0.137
	Mn$_1$ 1 a	Mn$_1$ 1 a	3.252						
	Ni$_1$ 3 c	Ni$_1$ 1 f	0.5						
		Ni$_2$ 1 d	0.555						
		Ni$_3$ 1 g	0.537						
CrFe$_2$Ni	*P4/mmm*	*Pm′m′m*		1.69		FiM	11.37		−0.026
	Cr$_1$ 1 c	Cr$_1$ 1 d	−2.436						
	Fe$_1$ 2 e	Fe$_1$ 1 g	2.046						
	Ni$_1$ 1 a	Fe$_2$ 1 f	2.123						
		Ni$_1$ 1 a	0.153						
CrMnNi$_2$	*P4/mmm*	*Pm′m′m*		1.47		FiM	11.6		−0.098
	Cr$_1$ 1 c	Cr$_1$ 1 d	−2.543						
	Mn$_1$ 1 a	Mn$_1$ 1 a	2.872						
	Ni$_1$ 2 e	Ni$_1$ 1 g	0.133						
		Ni$_2$ 1 f	0.338						
Cr$_2$FeMnNi$_4$	*I4/mmm*	*P-1*		1.36		FiM	11.49		−0.068
	Cr$_1$ 4 c	Cr$_1$ 1 g	−2.529						
	Fe$_1$ 2 a	Cr$_2$ 1 f	−2.539						
	Mn$_1$ 2 b	Fe$_1$ 1 b	2.432						
	Ni$_1$ 8 f	Mn$_1$ 1 h	2.856						
		Ni$_1$ 1 a	0.147						
		Ni$_2$ 1 d	0.109						

TABLE II. (*Continued.*)

Composition	Symmetry, WP	Mag. symm., WP	MM_{WP}, (μ_B)	AMMM, (μ_B) Current	Exp.	Magnetic ordering	Vol./at. (Å³) Current	Exp.	H_{form} (eV)
		Ni_3 1 e	0.146						
		Ni_4 1 c	0.113						

[a]Jung [118].
[b]Takano and Chikazumi[119].
[c]Owen *et. al* [120].
[d]Shull and Wilkinson [93].
[e]Reck and Fry [121].
[f]Wakelin and Yates [122].
[g]Bhatia *et. al* [123].
[h]Kren *et. al* [90].
[i]Kasper and Kouvel [95].
[j]Pearson *et. al* [89].
[k]Gokcen [87].
[l]Paoletti and Ricci [92].

a magnetic moment of 0.53 μ_B, which closely corresponds to the experimental measurements from Ref. [93] with $\mu_{Mn} = 3.18 \mu_B$ and $\mu_{Ni} = 0.3 \mu_B$, Ref. [91] with $\mu_{Mn} = 3.7 \mu_B$ and $\mu_{Ni} = 0.6 \mu_B$, and Ref. [92] with $\mu_{Mn} = 3.6 \mu_B$ and $\mu_{Ni} = 0.31 \mu_B$. Total AMMM of 1.21 μ_B is also very close to the experimental value of 1.1 μ_B from Ref. [92].

C. Ternary subsystems

In this subsection, the results of DFT calculations at 0 K for Fe-Cr-Mn, Fe-Mn-Ni and Cr-Mn-Ni ternary systems and the underlying binaries are presented and analyzed. Since the methodology and the results for the Fe-Cr-Ni ternary system are similar to the one used in Ref. [22], it is presented in the Supplemental Material [39], Sec. SIA.

Enthalpies of formation, enthalpies of mixing, volumes per atom and AMMMs for all ternary alloys are presented as color-coded ternary diagrams, where color represents values of a property of choice and three axes correspond to the concentrations of respective chemical elements. In such a representation, only one value for each composition can be presented, which is chosen to be the value of the most stable structure for each composition on all ternary plots. Values in between are interpolated to give a more readable picture.

In Refs. [13,14] it has been shown that the relative stability of lattice structures can be roughly estimated using VEC. With the change of VEC in the alloy, different phases show the dominant stability: bcc and other complex phases (e.g., Laves or σ phase) for VEC < 7; coexistence of bcc and fcc phases at 7 < VEC < 8; fcc phase for VEC > 8. Therefore, these critical values will be evaluated from the point of view of the phase stability obtained from the current DFT calculations.

1. Fe-Cr-Mn ternary

There are three ternary GSs in terms of enthalpy of mixing: $FeCr_4Mn$, which has a similar structure to the one of alloys of Fe with various elements from Ref. [99]; Fe_5Cr_2Mn, which is a derivative of $L1_2$ [99]; and Fe_6CrMn, which is the ABC_6-type structure, observed previously in $CuMnPt_6$ [100,101] that evolved through Cu_3Au-type alloy, in $Cu[Mn,Fe]Pd_6$ [102] and in Ni_6SiTi [103]. In terms of enthalpy of formation,

there are no GSs, and in general, the structures are less stable in the Cr-rich region [see Fig. 6(b)]. It should be noted that the structures with the highest H_{form} are observed for the compositions with VEC smaller than 7 [see a gray dash-dotted line in Fig. 6(b)], which confirms the RBA prediction of the instability of fcc structures with VEC smaller than 7.

No stable ternary Fe-Cr-Mn fcc intermetallic phases are found in literature [104]. Metallographic analysis, x-ray diffraction and electron probe micro analysis results show that the single-phase region of the fcc phase is only extended up to 5 at. % Cr and up to 38 at. % Mn in the ternary phase diagram at 923 K, whereas for Mn content less than 25 at. % the coexistence of fcc and fcc+σ phases is observed [105].

The Cr-rich region, limited at 70 at. % Cr on Cr-Mn edge and 30 at. % Cr on the Fe-Cr edge shows NM ordering, and the rest of the alloys show FiM ordering [see Fig. 6(c)]—the separation lines are shown by green dashed lines, which are constrained on ends (binary edges) by the compositions of DFT calculated structures.

Volume-concentration dependency for the Cr-rich NM region strongly corresponds to the Vegard's law estimate for NM references, whereas for FiM region the volume per atom increases with AMMM of the alloy and it has the highest values in the Fe-rich region [see Fig. 6(d)]. The concentration dependency behavior of studied parameters resembles the interpolation of binary subsystems plots.

2. Cr-Mn-Ni ternary

Trends in the stability of structures from the point of view of H_{form} are in accordance with the estimates from VEC [13,14]: the least stable structures are the ones having VEC lower than 7 [see a gray dash-dotted line in Fig. 7(b)], and the structures that have negative formation enthalpy are observed in the region of structures with VEC higher than 8 [see a gray dashed line in Fig. 7(b)]. Structures in between have positive formation enthalpy with the values close to 0.

The ternary GS in terms of enthalpy of mixing and enthalpy of formation [see Figs. 7(a) and 7(b)] is $CrNi_2Mn$, which was not found in literature, and has the same space group ($P4/mma$). Its magnetic space group ($Pm'm'm$) is the same
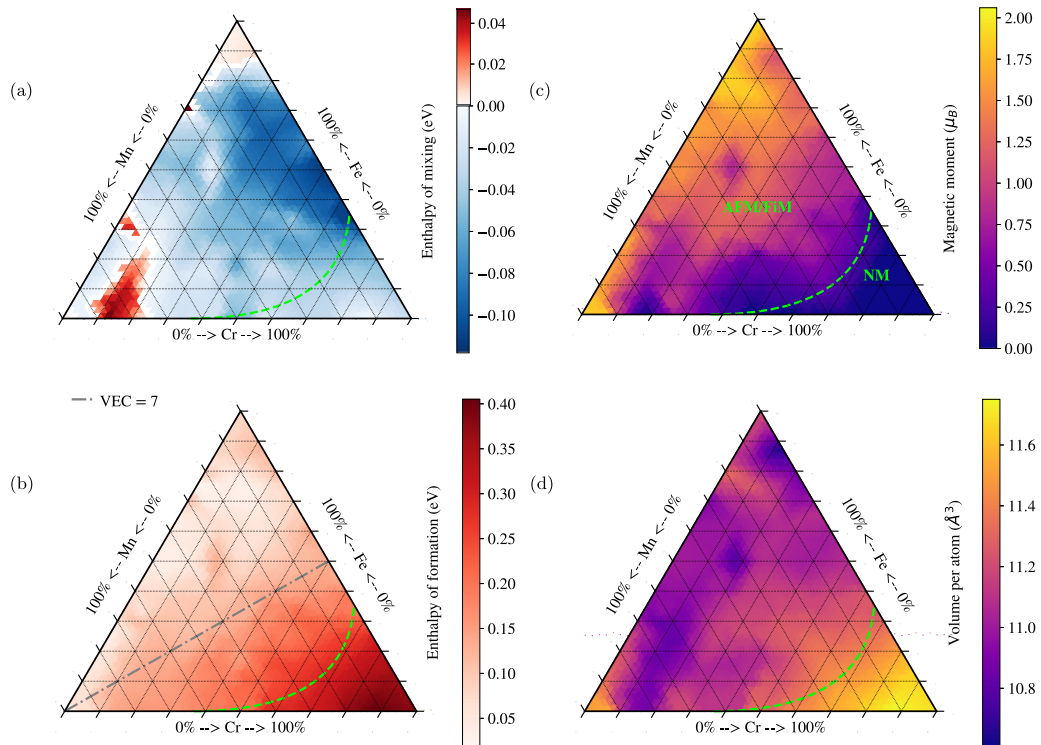
FIG. 6. Interpolated DFT results for the most stable structures and magnetic configurations for Fe-Cr-Mn alloys on fcc lattice: (a) enthalpy of mixing; (b) enthalpy of formation; (c) average magnitudes of magnetic moments; and (d) volume per atom. Green dashed lines separate the regions with different predominant magnetic configuration, which are indicated in (c). Gray dash-dotted line indicates the concentrations where VEC = 7; the region below the line has lower VEC and the region above it has higher VEC; VEC for pure Fe is 8.
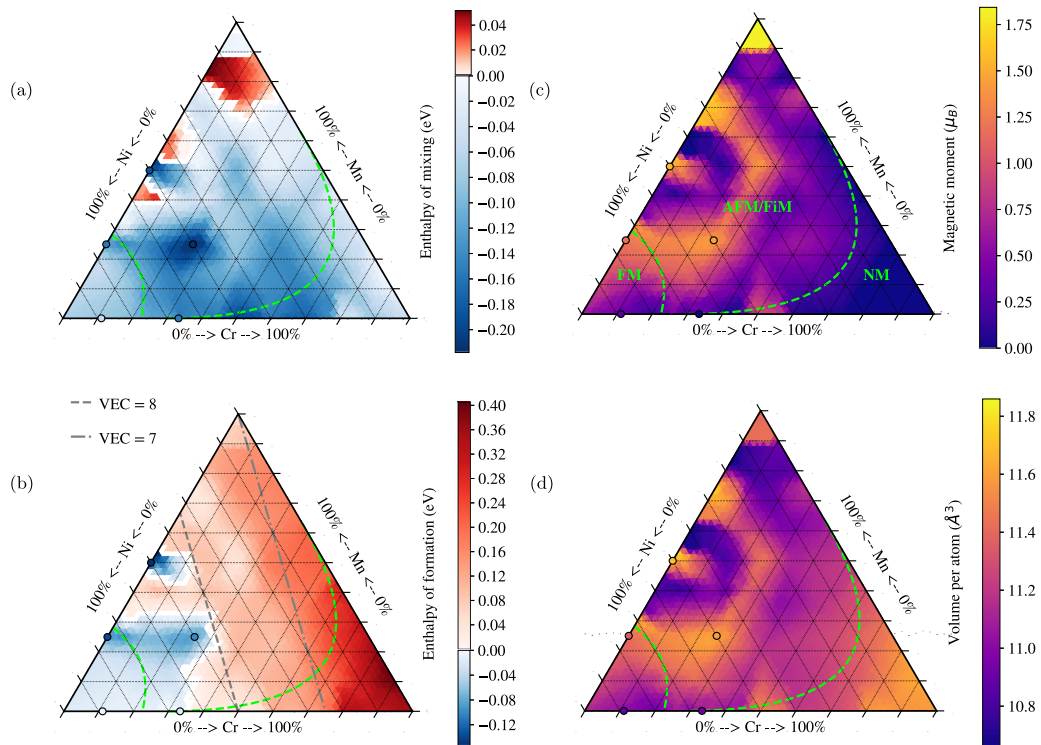

FIG. 7. Interpolated DFT results for the most stable structures and magnetic configurations for Cr-Mn-Ni alloys on fcc lattice: (a) enthalpy of mixing; (b) enthalpy of formation; (c) average magnitudes of magnetic moments; and (d) volume per atom. Green dashed lines separate the regions with different predominant magnetic configuration, which are indicated in (c). Filled circles represent GSs. Gray dashed line indicates the concentrations where VEC = 8 and gray dash-dotted line, where VEC = 7. The region on the right side has lower VEC and the region on the left side has higher VEC. VEC for pure Cr is 6 and for pure Ni is 10.
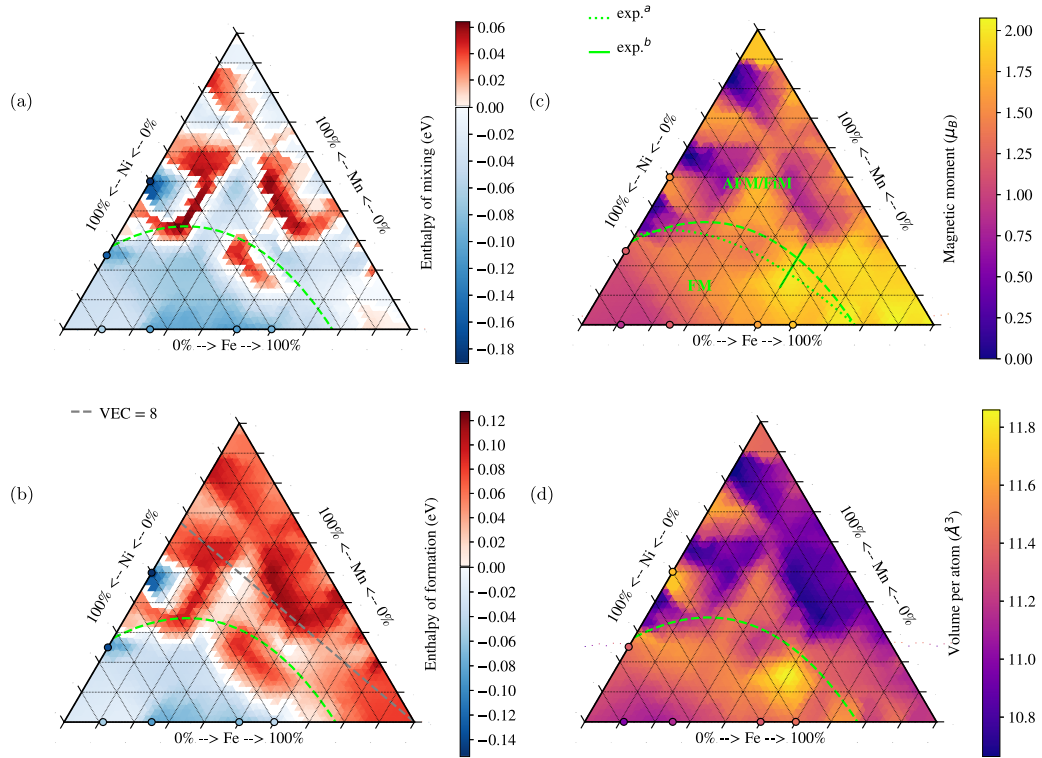
FIG. 8. Interpolated DFT results for the most stable structures and magnetic configurations for Fe-Mn-Ni alloys on fcc lattice: (a) enthalpy of mixing, (b) enthalpy of formation, (c) average magnitudes of magnetic moments, and (d) volume per atom. Green dashed lines separate the regions with different predominant magnetic configuration, which are indicated in (c). Filled circles represent GSs. Experimental data are adapted from the following: [a]Menshikov *et al.* [110] (the line that separate the regions of FM and AFM stability) and [b]Ettwig and Pepperhoff [112] (line of FM-AFM magnetic phase transition with the change of Ni concentration). Gray dashed line indicates the concentrations where VEC = 8; the region above the line has lower VEC and the region below it has higher VEC. VEC for pure Mn is 7 and for pure Ni is 10.

as in the previously predicted Fe_2CrNi phase from Ref. [22] (see Table II), although the relative magnitudes of magnetic moments are different: In Fe_2CrNi, the AMMM of Cr (1d) is the highest, 2.44 μ_B, followed by Fe (1g and 1f) with values 2.05 μ_B and 2.12 μ_B, and Ni (1a) having the lowest AMMM of 0.15 μ_B; and in $CrMnNi_2$ the highest value of magnetic moments is held by Mn (1a), equal to 2.87 μ_B; 1d is similarly occupied by Cr with AMMM of 2.54 μ_B; 1g and 1f are occupied by Ni atoms with the values of magnetic moments equal to 0.13 μ_B and 0.34 μ_B, respectively. Since ordered ternary structures with negative formation enthalpy were not found in Fe-Cr-Mn and Fe-Mn-Ni systems, and the previously predicted $FeCrNi_2$ has higher H_{form} than $CrNi_2Mn$, this makes $CrNi_2Mn$ is the most stable ordered ternary phase in the Fe-Cr-Mn-Ni. Ternary GS $CrNi_2Mn$ and GSs of underlying binary subsystems are marked on Fig. 7 as filled circles.

The Cr-Mn-Ni system has three regions of magnetic ordering [see Fig. 7(c)]—NM in Cr-rich region, limited at 70 at. % Cr in ternary ($Cr_{70}Mn_{15}Ni_{15}$), 30 at. % Cr at Cr-Mn binary and 50 at. % at Cr-Ni binary; FM in Ni-rich region, limited at 50 at. % Ni in Cr-Ni binary and 30 at. % Ni at Mn-Ni binary; and the rest of alloys are ordered as FiM—all indicated by green dashed lines. Values of volumes per atom in the NM region correspond to the Vegard's law estimate for NM references in the Cr-Mn region and are underestimated for Ni-rich region [see Fig. 7(d)]. Volume per atom in FM and FiM regions increases with the increasing average magnitude of magnetic

moment per atom in the alloy. The concentration dependency behavior of studied parameters resembles the interpolation of binary subsystems plots.

3. Fe-Mn-Ni ternary

In terms of enthalpy of mixing there is one ternary GS, fcc $FeMnNi_6$ (Fm-3m) [see Fig. 8(a)]. However, none of the structures is GS in terms of formation enthalpy. Ground states of underlying binary subsystems are indicated by filled circles on all subplots of Fig. 8. In general, structures with a negative enthalpy of formation are located in the Ni-rich region, due to the presence of fcc stabilizing Ni in sufficient concentrations [see Fig. 8(b)]. In this ternary system, the structures with negative formation enthalpy are also located only in the region with VEC more than 8, but the structures with very positive values of formation enthalpies can also be found in this region. This can be related to the: (i) incompleteness of the database (the structures with negative formation enthalpies for the chosen compositions may have not been predicted within the current model) or (ii) the fact that the VEC estimate is the empirical criteria, related to the stability of the experimentally observed HEAs at finite temperature, which means that the ordered structures with VEC more than 8 and positive formation enthalpy can decompose into more stable fcc phases observable at finite temperatures.
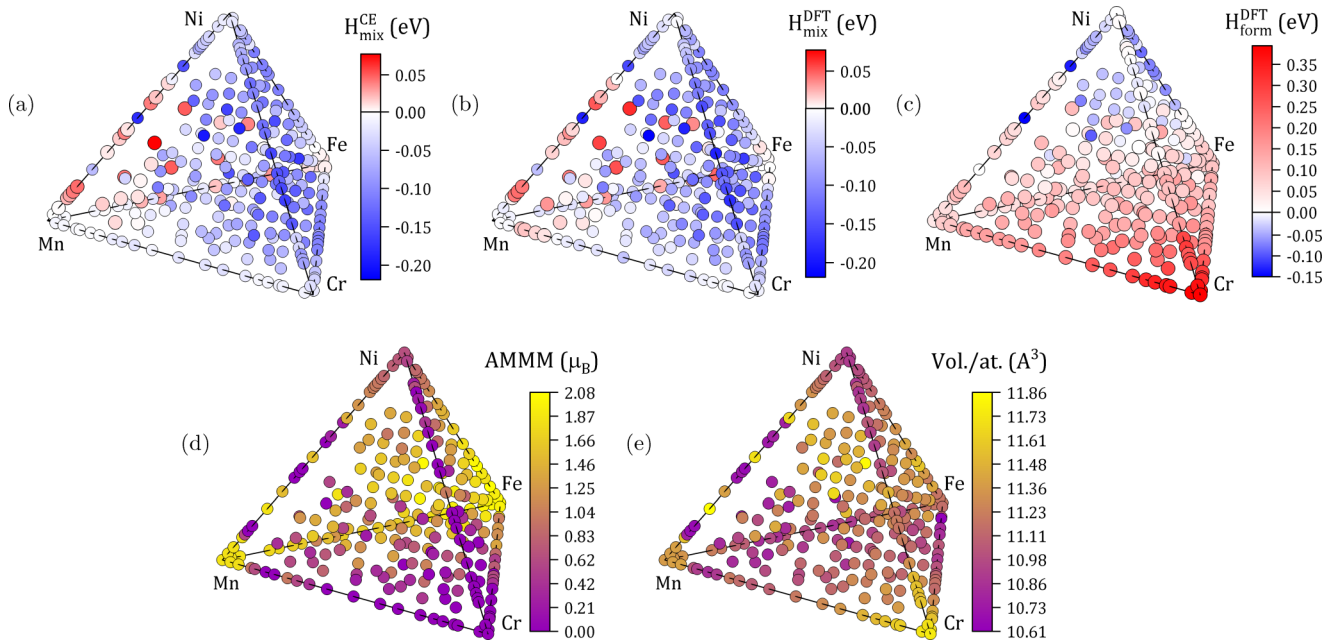
FIG. 9. The most stable structures for each considered composition calculated using DFT for Fe-Cr-Mn-Ni quaternary alloys and the underlying ternary and binary alloys on fcc lattice: (a) enthalpy of mixing from CE; (b) enthalpy of mixing from DFT; (c) enthalpy of formation from DFT; (d) average magnitudes of magnetic moments; and, (e) volume per atom.

Average magnitudes of magnetic moments from current calculations are compared to the neutron diffraction data from Refs. [106,107] for alloys with composition $Fe_{75-x}Ni_xMn_{25}$, $x = 0$–25 at. %. AMMM for FM and FiM structures, obtained in current work, lie between AMMM for AFM structures at 77 K and paramagnetic structures.

Aging experiments for $Fe_{75}Ni_{20}Mn_5$ [108] and $Fe_{7.8}Mn_{8.2}Ni_{84}$ [109] have indicated the low-temperature precipitation of the L1$_0$ MnNi and L1$_2$ MnNi$_3$ phases, which are the most stable ordered binaries in the Fe-Mn-Ni system.

Magnetic stability is divided into two regions [see Fig. 8(c)]: FM-ordered Ni-rich region, limited at 50 at. % Ni in ternary ($Fe_{25}Mn_{25}Ni_{50}$) and 40 at. % Ni at Fe-Ni binary, and the FiM-ordered region for the rest of the alloys (all regions are indicated by green dashed lines). Theoretical results are in a good correspondence with the experimental magnetic phase diagram for ternary [110,111] and pseudobinary $Fe_{50}Ni_xMn_{50-x}$, $x = 9.88$–39.74 at. % [112]. The lines separating the regions of stability of FM and AFM, presented in Fig. 8(c), are in good agreement with the separation line obtained experimentally at 4 K in Ref. [110] [indicated as a green dotted line in Fig. 8(c)] and the experimental line of phase transition with changing Ni concentration from Ref. [112] [indicated as a solid green line in Fig. 8(c)]. The AFM L1$_0$ MnNi structure has a very negative enthalpy of formation, which also corresponds to the ordered MnNi region in Ref. [113].

Since Fe-Mn-Ni ternary is fully magnetic, the volume per atom values are overestimated compared to the Vegard's law estimate and tend to increase with the increasing AMMM [see Fig. 8(d)]. The x-ray diffraction results for induction-melted specimens with varying composition $Fe_{75-x}Ni_xMn_{25}$, $x = 0$–25 at. %, annealed for 15 h at 900°C and water quenched [107], indicate that all three-component specimens have the disordered fcc lattice with the average volume per atom of 11.69 Å^3, which is close to the results of current calculations, 11.33 Å^3.

D. Fe-Cr-Mn-Ni quaternary system

Since DFT calculations in current studies give the results for 0 K and do not take the pressure into account, the concentration dependence of any chosen property can be represented analogously to how it has been done for ternary systems—as a color-coded diagram showing dependency on the concentration of four components. In the authors' opinion, the most representative way to illustrate the varying concentration of four components is the tetrahedron representation, where each vertex corresponds to the concentration of a considered element. The transformation of tetrahedral four-component coordinates into 3D Cartesian coordinates have been worked out in Refs. [114,115]. In such a representation, similarly to a ternary case, only one value per composition can be represented, and therefore, in the following plots only values for the most stable structures for each composition are shown.

Quaternary GS in terms of both mixing and formation enthalpies [see Figs. 9(a) and 9(c)] is FeCr$_2$MnNi$_4$ (*I4/mmm*), which was not found in literature, with the structure being the derivative of previously described ABC$_6$ type. Its atomic and magnetic configuration is illustrated in Fig. 10. Cr atoms are ordered as simple cubic structure, Fe and Mn atoms are ordered as fcc and Ni atoms show the layered structure with fcc[100] ordering within the layer.

Transmission electron microscopy of $Fe_{10}Ni_7Mn_6Cr_{77}$ (wt.%) alloy shows the pronounced precipitation within martensite and degenerate precipitation within the retained austenite [116]. Single-phase fcc near-equiatomic [FeNiMn]$_{82}$Cr$_{18}$ alloy was obtained with the arc-melting and
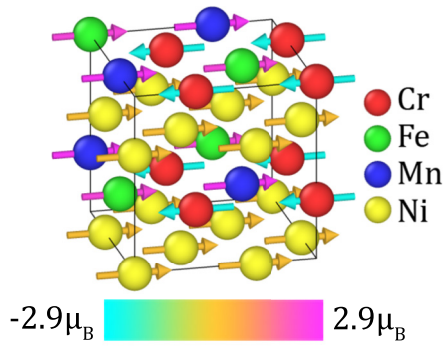
FIG. 10. Atomic structure of the predicted quaternary GS $FeCr_2MnNi_4$ in a conventional fcc unit cell.

homogenization, and remained stable under deformation [16]. AFM austenitic state is observed for $Fe_{61.5}Mn_{23}Ni_7Cr_{8.5}$ alloy [117].

Region of fcc stability from the points of view of the negative formation enthalpy is close to the estimate of a higher limit of fcc stability from the point of view of VEC (8 valence electrons per atom). This region is localized near the Ni corner, and for the quaternary and most underlying subsystems the Ni concentration should be 25 at. % at minimum, with the exception of the following: 40 at. % Ni for Fe-Ni binary; 50 at. % Ni for Cr-Mn-Ni ternary; and 67 at. % Ni for Cr-Ni binary.

Quaternary alloys in the middle of the phase diagram, where the concentration of every constituting element is larger than 12.5 at. %, show FiM ordering, and the alloys near the faces of the phase diagram show the ordering of neighboring lower-compound structures, with small NM region in Cr-rich part, limited at 62.5 at. % Cr in the quaternary $(Cr_{62.5}[FeMnNi]_{37.5})$ [see Fig. 9(d)]. The magnetic ordering of the most stable structures at each concentration was analyzed. The resulting 264 data points in the whole concentration range were interpolated to produce a theoretical magnetic phase diagram of the fcc Fe-Cr-Mn-Ni system, which is presented
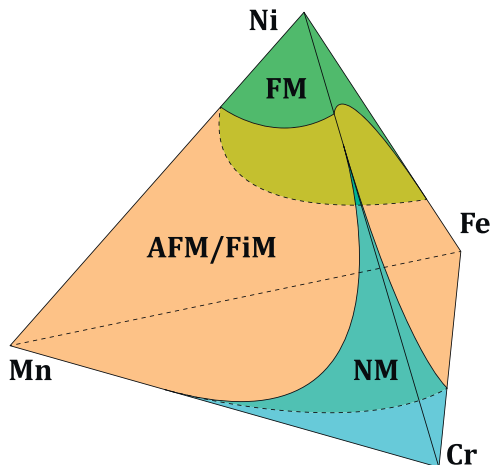

FIG. 11. Theoretical magnetic phase diagram of quaternary fcc Fe-Cr-Mn-Ni alloys based on the results of DFT calculations.

TABLE III. Number of structures used in CE for each subsystem and the respective CVSs. For K-component systems with $K > 2$, the number of structures with respective K elements is indicated in brackets.

System	No. of structures	CVS (meV)
CrFe	58	11
CrMn	55	8
CrNi	77	12
FeMn	58	12
FeNi	54	10
MnNi	52	12
CrFeMn	260 (89)	12
CrFeNi	274 (85)	12
CrMnNi	249 (66)	13
FeMnNi	219 (46)	12
FeCrMnNi	831 (191)	13

in Fig. 11. It should be noted that all the studied structures are ordered atomic structures with relatively high symmetry.

Values of volumes per atom [see Fig. 9(e)] have a positive correlation with the values of AMMM for the FiM region, observed in the major part of the quaternary system. AMMM and volume per atom from all studied binary, ternary and quaternary structures with VEC larger than the critical value of ~7 from Refs. [13,14] have been collected to illustrate the magneto-volume relation. This is represented in Fig. 12 and it is clearly seen that the volume per atom is increasing with the increase of the average magnitude of magnetic moments for all subsystems and quaternary system. However, for the Fe-Cr-Ni ternary subsystem, the rate of this change is the biggest. This means that AMMMs are strongly affected by the change of volume, compared to other subsystems. This fact may be responsible for the high swelling effect of Fe-Cr-Ni alloys. Also, since this linear magneto-volume relationship trend is weaker in Fe-Cr-Ni-Mn alloys in a comparison with those in the ternary Fe-Cr-Ni system, it supports the results of reduced swelling in Fe-Cr-Mn-Ni HEA compared to Fe-Cr-Ni in Ref. [9].

The enthalpy of formation, volume per atom, average magnitudes of magnetic moments, type of magnetic ordering, as well as crystallographic symmetry and magnetic symmetry for the most stable intermetallic structures of Fe-Cr-Mn-Ni alloys with negative formation enthalpy are given in Table II. The structures with positive formation enthalpy, which form the rest of the convex hulls with fcc references, are presented in Supplemental Material [39], Table SII.

E. Cluster expansion summary

CE has been constantly updated and the DFT results for the final databases have been discussed above. The number of structures used in the Fe-Cr-Mn-Ni system and each subsystem involved in the final mappings of H_{mix} from DFT to CE as well as the cross-validation scores are presented in Table III.

The differences between DFT and CE enthalpies of mixing for the most stable structures of all studied compositions can be compared in Figs. 9(a) and 9(b). These differences for all structures in binary subsystems are shown in the
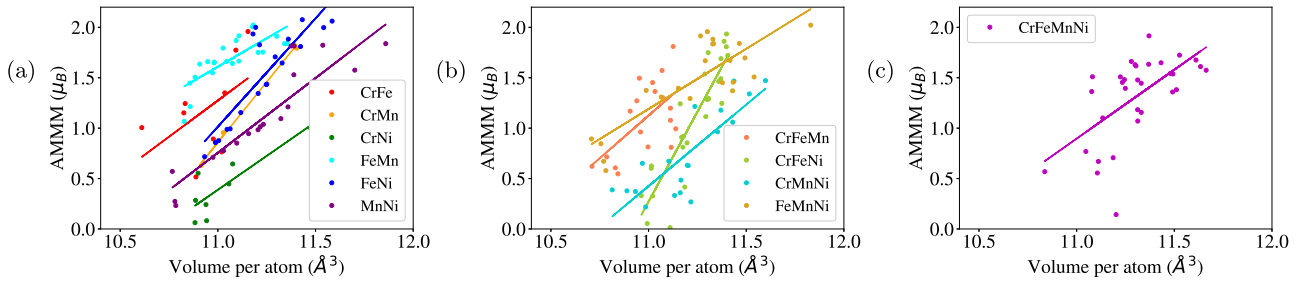
FIG. 12. Magneto-volume relation for (a) binary; (b) ternary and (c) quaternary alloys based on DFT calculations for structures with VEC > 7. Filled circles represent the most stable structures for each composition; solid lines represent the line fitting for the most stable structures.

Supplemental Material [39], Fig. S1 and for the most stable structures in ternary subsystems in Figs. S2–S5.

A chosen set of undecorated clusters (6 two-body, 2 three-body, and 1 four-body), uniform for each studied system, gives for binaries the same numbers of the decorated clusters. For ternaries, it gives 18 two-body, 10 three-body, and 5 four-body decorated clusters. Finally, for the quaternary system, it gives 36 two-body, 28 three-body, and 15 four-body decorated clusters. Exact values of ECIs for all binary, ternary and quaternary systems are given in Table I and are illustrated in Supplemental Material [39], Figs. S7, S8, and S9, respectively.

All theoretical and experimental fcc GSs and metastable phases within the Fe-Cr-Mn-Ni system have been reproduced in the final CE database. Moreover, two GSs have been predicted that are not found in literature—ternary $CrMnNi_2$ and quaternary $FeCr_2MnNi_4$—both with strongly negative H_{form} (see Table II). Magnetic properties show the same qualitative behavior as the experimental data and very close quantitative values of AMMMs. Finally, the CVS of 13 meV, achieved with the chosen set of clusters, is much smaller than the mixing enthalpies of GS and is considered to be reasonable.

The aforementioned facts support the validity of this cluster expansion model. Thus, the final ECIs for the quaternary fcc Fe-Cr-Mn-Ni (see Fig. S9 and Table I) are used in Monte Carlo simulations to predict the phase stability, configurational entropy, short-range order, and order-disorder transitions in Fe-Cr-Mn-Ni at finite temperatures, as described in the following section.

IV. FINITE-TEMPERATURE PHASE STABILITY OF FE-CR-MN-NI ALLOYS

The finite-temperature phase stability of Fe-Cr-Mn-Ni alloys was investigated with the semicanonical Monte Carlo simulations using ECIs obtained from the combination of CE and DFT calculations. MC simulations were performed for the 264 different compositions in the whole concentration range in the 10 at. % concentration mesh.

As a result of MC simulations, the mixing enthalpies and the many-body probability functions have been obtained. The latter have been subsequently used in order to calculate the configurational entropy and the Warren-Cowley SRO parameters.

Order-disorder transition temperature (T_{ODT}) in the current work was identified as the temperature above which the system is disordered and below which the system shows partial ordering. The chemical ordering strongly affects both the enthalpy of mixing and the configurational entropy of mixing of the studied system. Therefore, the thermodynamic potential which includes both these values, such as free energy of mixing, would accurately represent the order-disorder transition. Hence, T_{ODT} in this work was identified via the inflection point on the curve of a free energy of mixing as a function of temperature, which refers to the change of sign of the second derivative of the free energy of mixing as a function of temperature. Taking into account the cross-validation error between the CE and DFT, 13 meV, the error margins of the predicted T_{ODT} can be estimated to be equal to 150 K.

Since MC simulations used in this work are based on the lattice gas model, they take into account neither the change of the state of matter nor the change of lattice. Therefore, all phase transitions are treated as ordering-related transitions, and the transition at the highest temperature for a chosen composition is interpreted as the order-disorder transition.

A. Configurational entropy calculation from a combined Monte Carlo and cluster expansion

Combining Monte Carlo simulations with the cluster expansion method is the common approach for calculating thermodynamic properties once ECIs, $J_{\omega,n}^{(s)}$, are known. Within the Monte Carlo technique, the free energies and mixing enthalpies are calculated for atomic configurations in the supercells at specific temperature ranges and chemical potentials using known energies from the cluster expansion model associated with clusters, and the other thermodynamic properties are calculated from these quantities.

Within the thermodynamic integration method, the configurational entropy is calculated as:

$$S^{conf}(T) = \int_0^T \frac{C^{conf}(T')}{T'} dT', \qquad (20)$$

where the configurational contribution to the specific heat, C^{conf}, is related to the fluctuations of the enthalpy of mixing, calculated within Monte Carlo at a given temperature [124,125] as:

$$C^{conf}(T) = \frac{\langle H_{mix}^2(T) \rangle - \langle H_{mix}(T) \rangle^2}{T^2}, \qquad (21)$$

where $\langle H_{mix}(T) \rangle$ and $\langle H_{mix}(T) \rangle^2$ are the mean and mean squared enthalpies of mixing, respectively, i.e., the numerator describes the variance of $H_{mix}(T)$.
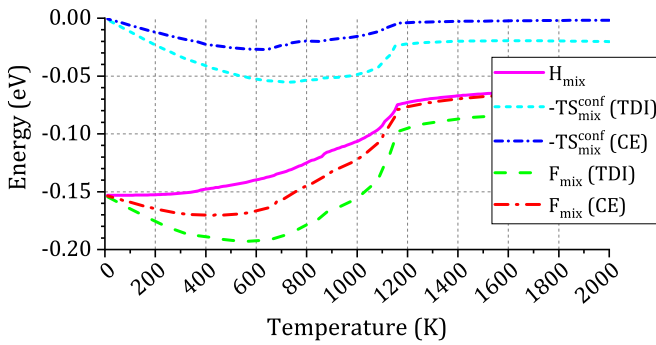
FIG. 13. Enthalpy of mixing and free energy of mixing from Monte Carlo simulations, as well as $-TS_{\mathrm{mix}}^{\mathrm{conf}}$ and free energies of mixing calculated using Thermodynamic Integration method and cluster expansion methods for the equiatomic Fe-Cr-Mn-Ni alloys.

However, in order to accurately perform the integration of a region around the transition temperature, which looks like a narrow peak on the function of $C^{\mathrm{conf}}(T)$, the simulations should be performed with a small temperature step, which increases the simulation time significantly. Therefore, the practical limitations for the Monte Carlo technique are time consuming simulations required for the Thermodynamic Integration method.

The cluster variation method (CVM) is a variational method where quantities such as entropy are formulated in terms of correlation functions, which are calculated from the function minimization. Since CVM uses analytical formulas, its limitation is the need to consider the clusters with many points. The configurational entropy corresponding to each of the 10 basic cluster obtained by the cluster expansion method, as well as the configurational entropy obtained from the Monte Carlo thermodynamic integration method, is presented and discussed in the paper of Fernández-Caballero *et al.* [35].

The entropy contribution from the most influential cluster obtained in Ref. [35], which happens to be the first nearest neighbor cluster, will be used in this paper including Fig. 13
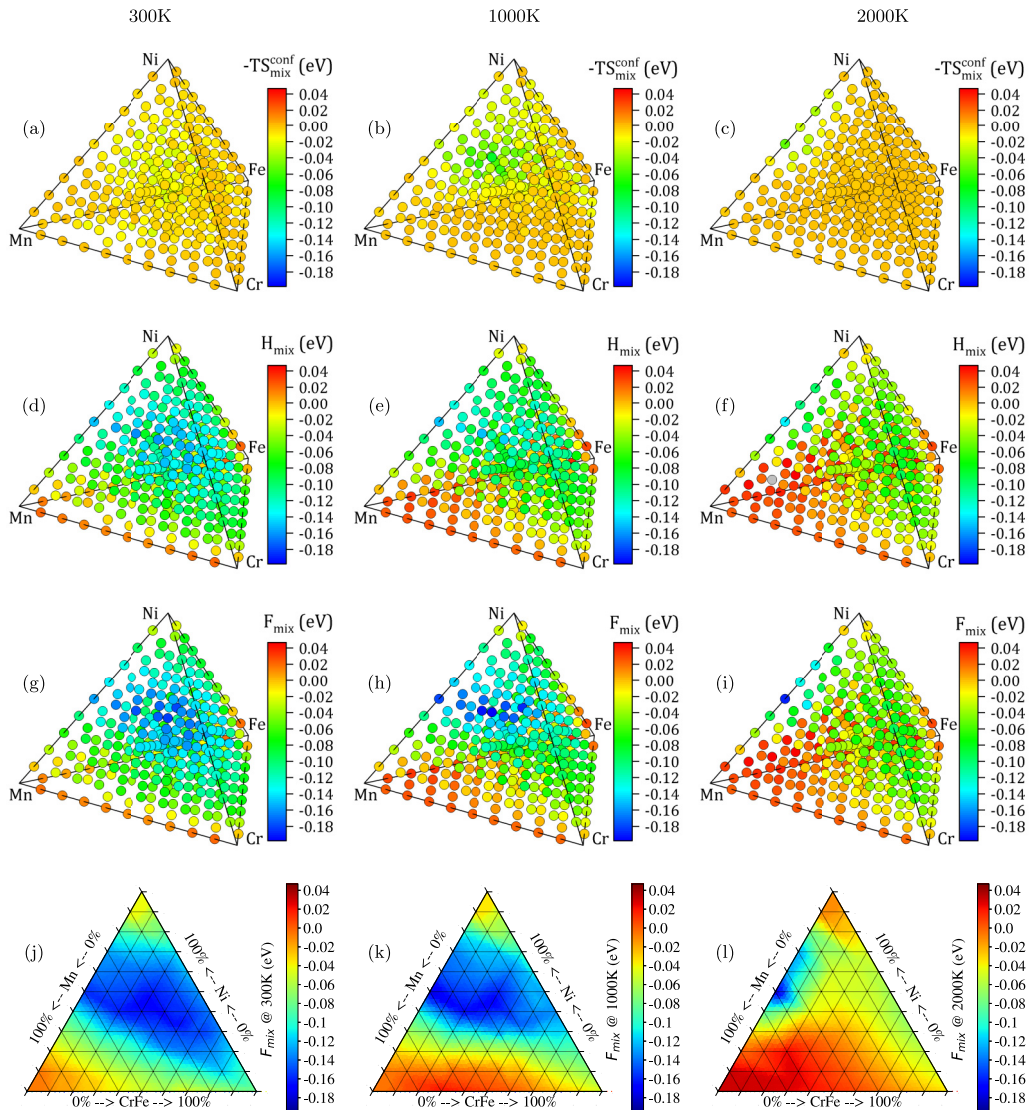
FIG. 14. Contribution of [(a)–(c)] $-TS_{\mathrm{mix}}^{\mathrm{conf}}$ and [(d)–(f)] H_{mix} to [(g)–(i)] F_{mix} in the whole concentration range at 300 K, 1000 K and 2000 K. S^{conf} is taken from the cluster $\omega = 2$, $n = 1$. Two-dimensional slice of F_{mix} [(j)–(l)], where Cr and Fe concentrations are equal.

and Fig. 14. It is expressed as follows:

$$
\begin{aligned}
S_{2,1}^{\text{conf}}(\vec{\sigma}) = &\, 11 \sum_s y_{1,1}^{(s)}(\vec{\sigma}) \ln\left[y_{1,1}^{(s)}(\vec{\sigma})\right] \\
&- 6 \sum_s y_{2,1}^{(s)}(\vec{\sigma}) \ln\left[y_{2,1}^{(s)}(\vec{\sigma})\right],
\end{aligned}
\tag{22}
$$

where $\vec{\sigma}$ dependence on the $y_{\omega,n}^{(s)}(\vec{\sigma})$ is introduced to indicate that the equilibrium configuration of the Monte Carlo supercell, $\vec{\sigma}$, is associated to the temperature, T.

In order to compare the results of the two methods of entropy calculations, Monte Carlo simulation with the thermodynamic integration routine has been performed for the equiatomic composition in a supercell of 8000 atoms starting from 3000 K down to 0 K considering 1000 equilibration steps and 2000 accumulation Monte Carlo steps per site at each temperature in steps of $\Delta T = 5$ K.

The configurational entropy obtained from the analytic formulation at temperatures in the range 0–1000 K is found to be sensitive to ECIs and the Monte Carlo calculation temperature step, resulting in nonphysical values of negative entropies for certain clusters.

In the high temperature limit, the expression of configurational entropy corresponding to each of the basic clusters and the one obtained from TDI are found to converge toward the perfect random solid solution (also known as the temperature independent Bragg-Williams approximation) for the average system composition, c_p, given by $S_{\text{ideal}}^{\text{conf}}(T) = -k_B \sum_p c_p \ln(c_p)$, which, in the case of equiatomic composition is equal to $1.386\, k_B$.

B. Free energy of mixing

Knowing the enthalpy of mixing and the configurational entropy, the free energy of mixing can be evaluated as $F_{\text{mix}}(T) = H_{\text{mix}}(T) - T S_{\text{mix}}^{\text{conf}}(T)$, where $S_{\text{mix}}^{\text{conf}}(T)$ is defined as $S_{\text{ideal}}^{\text{conf}} - S_{\text{real}}^{\text{conf}}(T)$. Example calculation for equiatomic composition is illustrated in Fig. 13, where the free energies of mixing obtained from the basic cluster approximation corresponding to the 1st nearest neighbor two-body cluster ($\omega = 2$, $n = 1$) and TDI calculations are presented.

It can be seen for the $-T S_{\text{mix}}^{\text{conf}}$ obtained from both CE and TDI methods (see Fig. 13), that its contribution to the free energy of mixing is very small in the high-temperature limit, which is related to the convergence toward the perfect random solid solution discussed above. On the other hand, for the temperatures below T_{ODT}, the contribution of $-T S_{\text{mix}}^{\text{conf}}$ becomes prominent and decreases the values of F_{mix} notably.

In order to demonstrate the contribution of $-T S_{\text{mix}}^{\text{conf}}$ to F_{mix} values in the whole range of compositions of Fe-Cr-Mn-Ni alloys, the tetrahedron representations of H_{mix}, $-T S_{\text{mix}}^{\text{conf}}$ and F_{mix} at 300 K, 1000 K, and 2000 K are shown in Fig. 14. It should be noted, that for a few compositions at 300 K the values of entropy obtained from CE were negative, and hence they are not represented on the corresponding subfigures of Fig. 14.

The values of $-T S_{\text{mix}}^{\text{conf}}$ at 2000 K are substantial mainly for the compositions with the high concentration of MnNi [see Fig. 14(c)]. At 1000 K, which is below T_{ODT} for the major part of the compositions in the middle of the phase diagram, the
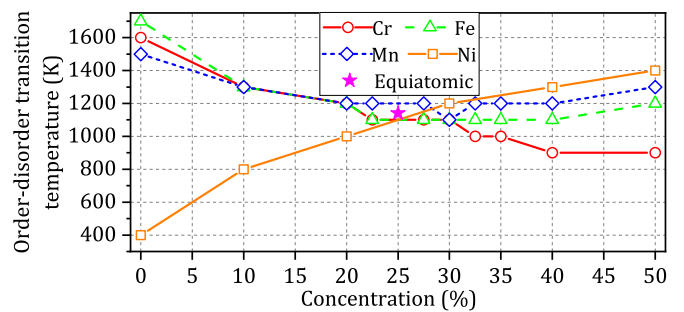

FIG. 15. Order-disorder transition temperatures as a function of each element concentration. Each data point represents different pseudobinary alloy, in which the concentration of a chosen element is equal to that on x axis and the relative concentration of other elements is equiatomic.

values of $-T S_{\text{mix}}^{\text{conf}}$ are substantial for these compositions [see Fig. 14(b)]. At 300 K, where ODT has occurred for almost all compositions, the values of $S_{\text{mix}}^{\text{conf}}$ are nonzero [see Fig. 14(a)]. However, since the temperature is comparatively small the $-T S_{\text{mix}}^{\text{conf}}$ is also smaller than at 1000 K.

Since H_{mix} has been obtained from the MC simulations, it shows a clear temperature dependence. At low temperature [see Fig. 14(d)], the majority of the compositions have negative H_{mix} with its values being strongly negative. When the temperature is increased [see Fig. 14(e) and 14(f)], the values of H_{mix} gradually become less negative, and for some compositions the H_{mix} becomes positive.

Due to the effect of both contributions, F_{mix} has a different dependence on temperature in different regions. For the compositions which are close to the vertices of the phase diagram, the trend in temperature dependence is similar to the trend in H_{mix}. On the other hand, the values of F_{mix} in the middle of the phase diagram are most negative at 1000 K [see Fig. 14(h)], being even more negative than at 300 K [see Fig. 14(g)], whereas at 2000 K, F_{mix} is strongly negative only for structures close in composition to MnNi [see Fig. 14(i)]. It should be noted that the effect of some structures being more stable at elevated temperatures than at lower temperatures can be caused by the constraints of the current work, where only the fcc lattice is considered, and the vibrational and magnetic contributions are not taken into account.

C. Order-disorder transition temperatures

Order-disorder transition temperature has been calculated for each MC simulated structure in the whole concentration range as the inflection point on the curve of the free energy of mixing versus the temperature for the given structure.

The effect of each element concentration on T_{ODT} has been studied on the pseudobinary compositions of type $A_x[BCD]_{(1-x)}$. The order-disorder transition temperatures as functions of concentration in pseudobinaries are shown in Fig. 15. T_{ODT} dependency on concentration for manganese has a minimum at 30 at. % Mn, which is 1100 K. T_{ODT} dependency on concentration for Fe has a minimum range of 22.5–40 at. % Fe with T_{ODT} in this range being equal to 1100 K. T_{ODT} as a function of Cr concentration decreases with increasing Cr concentration similar to Fe up to 30 at. % Cr and
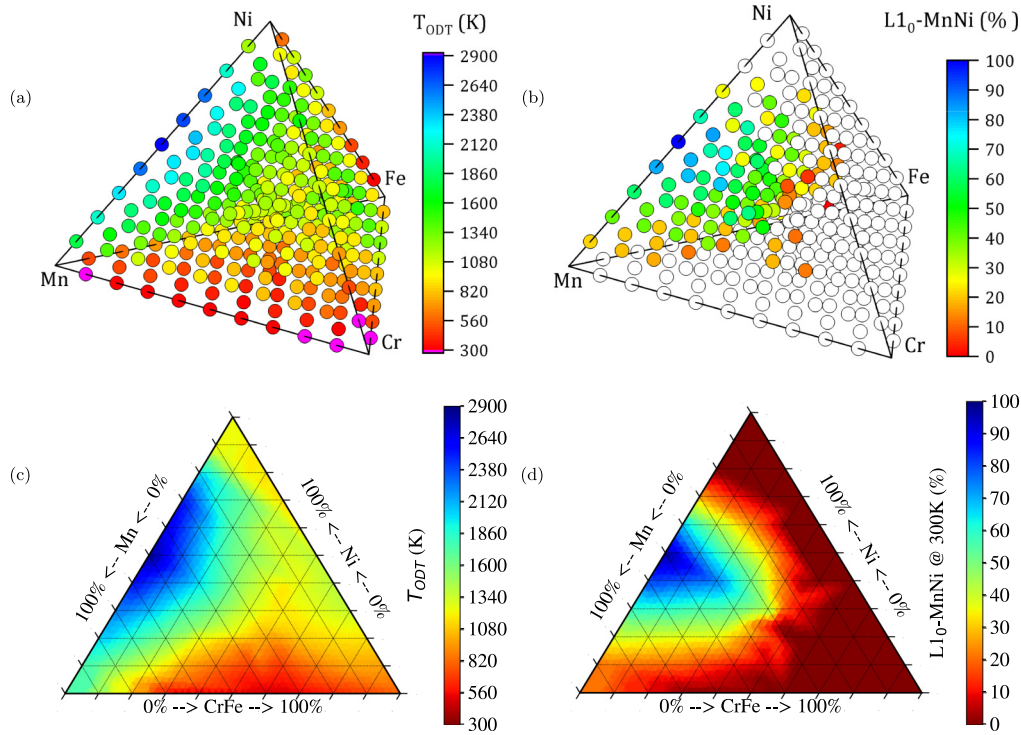
FIG. 16. (a) Order-disorder transition temperatures for the whole concentration range of Fe-Cr-Mn-Ni alloys; (b) a percentage of AFM $L1_0$-MnNi precipitate at 300 K in the whole concentration range, as well as [(c) and (d)] respective 2D slices where Cr and Fe concentrations are equal.

then continues to decrease. One of the possible explanations of such behavior is that Cr at large concentrations suppresses the magnetic moments of other elements, decreasing the influence of magnetic interactions on the ordering. Also, there are no GSs with negative formation enthalpy and Cr content more than 33.3 at. %, which would require more time for atoms to reallocate themselves to the positions of preferable precipitates. Nickel pseudobinary is the most interesting because Ni is fcc-stabilizer, and T_{ODT} as a function of its concentration, as opposed to other elements, increases monotonically with increasing Ni concentration. Hence, the smallest T_{ODT} equal to 400 K is observed for equiatomic fcc FeCrMn alloy without Ni and VEC = 7, and its stable lattice is most likely not fcc.

The order-disorder transition temperature as a function of concentration of each element in Fe-Cr-Mn-Ni alloys for the structures from a concentration mesh and pseudobinaries is presented in Fig. 16(a). It can be seen from this plot that the lowest temperatures of order-disorder transitions are observed in the structures with the lowest Ni concentration, exactly what is observed in the pseudobinaries. It should be noted that Ni is the fcc stabilizer and that alloys with small Ni concentration, which in this system corresponds to small VEC, may transform into the non-fcc phase. Therefore the Ni content should be balanced accurately to achieve the disordered fcc single-phase composition.

In current calculations, the ORNL alloy [9] with composition $Cr_{18}Fe_{27}Mn_{27}Ni_{28}$ during the cooling is disordered above 1290 K. Below that temperature, the $L1_0$ MnNi phase starts to form [see representative structures in Fig. 17(c)].

The value of $T_{ODT} = 1290$ K is lower than the temperature of the samples homogenization of 1473 K from Ref. [9], but it is higher than the temperature of recrystallization of 1173 K from the same Ref. [9], after which its authors report the single-phase fcc structure. Taking into account the error of 150K, which propagated from CE, the T_{ODT} values are similar. It should be noted again that the current simulations do not take into account the effect of lattice vibrations on the evolution of the structure, which, if accounted for, may contribute to the lowering of T_{ODT}.

It should be noted that the authors of experimental Ref. [9] state that according to the exploratory studies, the equiatomic alloy does not form fcc single-phase structure and the composition which does form it is $Cr_{18}Fe_{27}Mn_{27}Ni_{28}$ (ORNL)—the alloy with near-equiatomic composition and depleted Cr concentration. This result is supported by the estimation of VEC, where fewer valence electrons per atom corresponds to the lower stability of the fcc lattice, and the value for equiatomic composition (7.75) is lower than for ORNL composition (7.93). In the current work, the formation enthalpy of the ORNL composition is more negative than that of equiatomic alloy in the whole studied temperature range [compare Figs. 17(c) and 17(e)]. The free energy of mixing at 1173 K is equal to -0.044 eV for equiatomic alloy and -0.150 eV for ORNL alloy.

Moreover, current MC simulations show that for lower temperatures, which are still located in the range of working temperatures for fusion reactors [126], the phase composition of the ORNL alloy is divided into distinct regions: one is the $L1_0$ MnNi precipitate and the other is a combination of the quaternary and Mn-/Ni-poor ternary phases. The precipitation
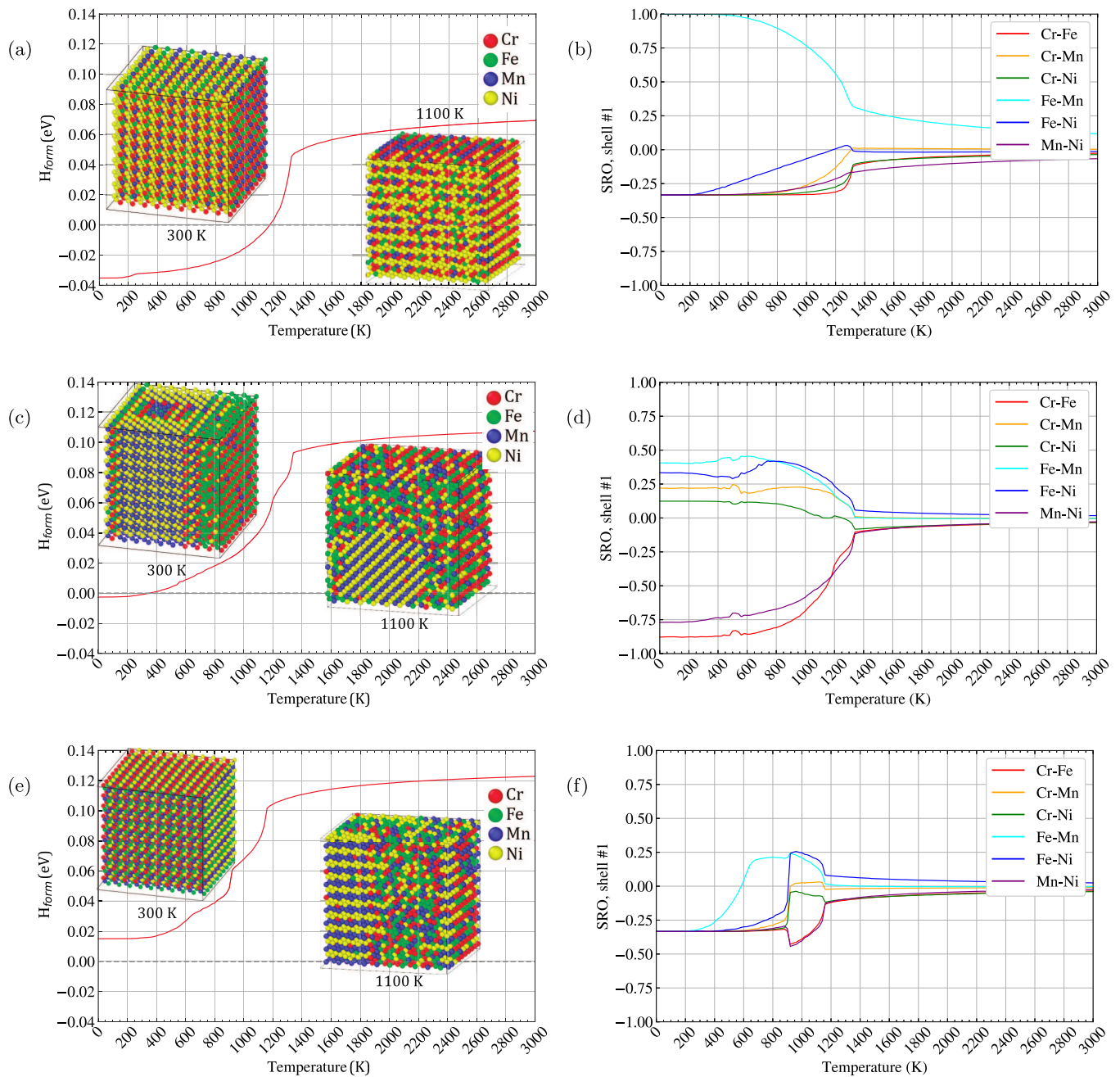
FIG. 17. Formation enthalpy obtained from the MC simulations and the SRO parameters in the first coordination shell for the $FeCr_2MnNi_4$ intermetallic phase [(a) and (b)], $Cr_{18}Fe_{27}Mn_{27}Ni_{28}$ [9] [(c) and (d)] and the equiatomic composition [(e) and (f)]. The representative structures of each alloy generated in MC simulations at 300 K and 1100 K are shown inside the figures.

of the $L1_0$ MnNi phase is in line with the Cantor alloy studies from Ref. [20], where it was one of the three major precipitates that formed after annealing for 500 days at 773 K.

$L1_0$-MnNi is the most stable structure, which has very strong short-range ordering (as discussed later), and Mn-Mn-Ni-Ni cluster has been shown to have the highest value of the cluster correlation function in Ref. [35]. Based on these facts, the analysis was made to find out the compositions, where $L1_0$-MnNi precipitates in the Fe-Cr-Mn-Ni quaternary system. Positions and types of atoms were taken from the MC simulations at temperature 100 K. The first nearest neighbors of each atom were analyzed and if at least one unit cell had

the structure of $L1_0$ (2 Mn atoms and 2 Ni atoms), the atom was indicated as belonging to $L1_0$ phase. Indication via the unit cell makes the analysis very computationally efficient and does not yield false positive errors, meaning that it does not indicate 1-layer Mn-Ni precipitates or Mn-Ni clusters which are part of more complex intermetallic compounds as Mn-Ni $L1_0$ phase. The percentage of $L1_0$-MnNi phase in the full concentration range of Fe-Cr-Mn-Ni is presented in Fig. 16(b).

When the region with precipitated $L1_0$-MnNi is compared to the order-disorder transition temperatures, a strong correlation is observed between the percentage of $L1_0$-MnNi in

low-temperature phase composition and T_{ODT} of the alloy [see Fig. 16(a)]: with an increasing percentage of $L1_0$-MnNi the values of T_{ODT} also increase. This can be interpreted as follows: If the concentration of Mn-Ni is more than 50 at. %, it allows the Mn and Ni atoms to be involved in the formation of $L1_0$-MnNi phase, which is a very stable ordered structure. Therefore, even at high temperature, when the other parts of an alloy may become disordered, $L1_0$-MnNi keeps its order, hence increasing T_{ODT} value of the alloy.

D. Short-range order parameters

The chemical SRO in the system was investigated in detail by analyzing the Warren-Cowley SRO parameters, calculated from Eq. (A7), derived from Eq. (8), using pair-correlation functions obtained from MC simulations. Inflection points on the Warren-Cowley SRO parameters as functions of temperature indicate the order-disorder transition temperatures, which are the same as the ones obtained from the analysis of mixing enthalpies (see Fig. 17 for exemplary comparisons).

As can be seen from Figs. 17(a) and 17(b), the quaternary GS shows simple behavior—it has one order-disorder transition temperature at 1300 K and all SRO pairs represent the chemical interactions in the quaternary GS below T_{ODT}. In the intermetallic phase at 0 K, the Cr atoms do not have Cr neighbors and are surrounded by two Fe atoms, two Mn atoms, and eight Ni atoms. Fe and Mn atoms do not have Fe and Mn neighbors and are surrounded by four Cr atoms and eight Ni atoms. Ni atoms are surrounded by four Cr, two Mn, two Fe, and four Ni atoms.

Composition of the ORNL sample undergoes two subsequent order-disorder transitions: first at 1320 K, when $L1_0$-MnNi starts forming, and second at 1180 K when $L1_2$-Fe_3Cr starts forming. Those order-disorder transitions are visible both on formation enthalpy as a function of temperature [see Fig. 17(c)] and SRO as a function of temperature [see Fig. 17(d)]. In the latter, it is also clearly seen that the Mn-Ni and Fe-Cr pairs drive the ordering.

The equiatomic composition also undergoes two subsequent order-disorder transitions—first at 1140 K, when $L1_0$-MnNi starts to form, similarly to the ORNL composition. During the second transition at 900 K, the already formed $L1_0$-MnNi phase rapidly dissipates and the environment becomes more uniform, which leads to the gradual formation of the ordered single phase [see Fig. 17(e)]. This rapid transformation is also represented by the rapid change of all SRO parameters [see Fig. 17(f)].

Comparing the results for ORNL and equiatomic compositions, it can be seen that the order-disorder transition is driven by the formation of $L1_0$-MnNi in both alloys and moreover, the behavior of SRO in the equiatomic alloy in the intermediate temperature range below T_{ODT} is similar to that in the ORNL alloy. However, below 900 K the behavior of SRO in the two alloys stops being similar. According to the analysis of the nearest neighbors, when the Mn and Ni atoms start to precipitate in the form of $L1_0$-MnNi, the rest of the composition space in ORNL alloy is close to that of $L1_2$-Fe_3Cr, the ordered metastable phase (see Fig. 20, Appendix C). This is represented in SRO for ORNL: Mn-Ni and Fe-Cr pairs show attraction, and others show repulsion. The situation

in the equiatomic alloy is different: The concentration of the Cr and Fe atoms in the alloy part, which is not involved in the formation of $L1_0$-MnNi, are similar. This means that in contrast to the ORNL alloy, there are more Cr atoms in the equiatomic alloy that can be attracted by Ni and Mn atoms. As can be seen in Fig. 17(f), the SRO parameters for Cr-Ni and Cr-Mn pairs are negative for the equiatomic composition, as opposed to the ORNL alloy.

The difference in SRO for ORNL and equiatomic alloys is most significant at low temperatures, but it is noticeable even above T_{ODT}. It means that most likely, the experimentally obtained alloys will have different properties to some extent. Hence, the extrapolation of the properties of the equiatomic alloy, as has been done in Ref. [12], might need a revision. Also, the influence of SRO on the defect properties, as the extension of the current work, may be of interest.

SRO obtained from MC simulations have been compared to experimental data for four alloy compositions: $Fe_{56}Cr_{21}Ni_{23}$, $Fe_{42.5}Cr_{7.5}Ni_{50}$, $Fe_{38}Cr_{14}Ni_{48}$, $Fe_{34}Cr_{20}Ni_{36}$ (see Supplemental Material [39], Fig. S11). Current results reproduce the previous simulations results [22] and are close to experimental values above 1000 K [127,128].

Analysis of the SRO parameters has been conducted for the $Ni_x[CrFeMn]_{(1-x)}$ pseudobinaries, studied with MC, and the results are presented in the Supplemental Material [39], Sec. SIID.

V. CONCLUSIONS

Stability of the quaternary Fe-Cr-Mn-Ni system and all underlying subsystems have been investigated in terms of enthalpies of mixing and enthalpies of formation using the density-functional theory. True fcc GSs have been found for binary and ternary subsystems containing Ni, and their existence is supported by the results of experiments and simulations reported in the literature. New fcc GSs, namely quaternary $FeCr_2MnNi_4$ and ternary $CrMnNi_2$, which were not previously described in the literature, are predicted to have negative formation enthalpy at 0 K. Ordered structures with negative formation enthalpies have been found only in the regions with the valence electron concentration higher than 8, which is consistent with the previous studies.

The theoretical magnetic phase diagram for the fcc Fe-Cr-Mn-Ni system, constructed based on the results of the current DFT calculations at 0 K, is shown to be consistent with the existing experimental data. The values of volumes per atom for structures with the valence electron concentration larger than 7 correlate with the values of AMMM—the higher values of AMMM correspond to the bigger volumes per atom. The effect of Mn is prominent in the magneto-volume relation, which supports the results of reduced swelling in Fe-Cr-Mn-Ni high-entropy alloys compared to Fe-Cr-Ni.

The calculation of configurational entropy using the TDI method and the analytical cluster variation method has shown that the latter nicely describes configurational entropy at high temperature and a little below order-disorder transition temperature, while not requiring additional computationally demanding calculations like TDI. Both methods show that the influence of configurational entropy is most prominent in

the intermediate temperature range, where the order-disorder transition occurs.

The analysis of the SRO parameters has indicated that the interaction between every two elements in the multicomponent system is a local property and depends on the atomic configuration around an atom at a given temperature. The difference in SRO between near-equiatomic $Cr_{18}Fe_{27}Mn_{27}Ni_{28}$ and equiatomic FeCrMnNi alloys at high temperatures results in a completely different atomic structure at low temperatures – phase separation with the pronounced precipitation of $L1_0$-MnNi in the former and the metastable ordered structure in the latter.

It has been found that the order-disorder transition temperature (T_{ODT}) of the system decreases with decreasing Ni concentration and increasing concentration of other elements. Stable intermetallics also increase T_{ODT}. The correlation has been indicated between T_{ODT} and the percentage of AFM $L1_0$-MnNi—the most stable ordered structure in the multicomponent Fe-Cr-Mn-Ni system—precipitated at low temperature.

As the continuation of the current work, the behavior under irradiation and the defect properties of equiatomic and near-equiatomic Fe-Cr-Mn-Ni alloys will be studied with a special interest in the magneto-volume effect and SRO influence on the defect migration.

APPENDIX A: DERIVATION OF SRO FROM MATRIX FORMULATION

In this work, τ_K matrices for $K = 2, 3, 4$ are defined as follows:

$$\tau_2 = \begin{pmatrix} 1 & 1 \\ -1 & 1 \end{pmatrix}, \quad \tau_3 = \begin{pmatrix} 1 & 1 & 1 \\ -1 & \frac{1}{2} & \frac{1}{2} \\ 0 & -\frac{\sqrt{3}}{2} & \frac{\sqrt{3}}{2} \end{pmatrix},$$

$$\tau_4 = \begin{pmatrix} 1 & 1 & 1 & 1 \\ -1 & 0 & 1 & 0 \\ 0 & -1 & 0 & 1 \\ -1 & 1 & -1 & 1 \end{pmatrix}. \tag{A1}$$

Three- and four-body correlation functions within the matrix formulation are defined as:

$$\left\langle \Gamma_{3,n}^{(s)} \right\rangle = \sum_{A,B,C} (\bar{\bar{\tau}}_K \otimes \bar{\bar{\tau}}_K \otimes \bar{\bar{\tau}}_K)_{(s),A,B,C} y_{3,n}^{ABC} \tag{A2}$$

and

$$\left\langle \Gamma_{4,n}^{(s)} \right\rangle = \sum_{A,B,C,D} (\bar{\bar{\tau}}_K \otimes \bar{\bar{\tau}}_K \otimes \bar{\bar{\tau}}_K \otimes \bar{\bar{\tau}}_K)_{(s),A,B,C,D} y_{4,n}^{ABCD}, \tag{A3}$$

respectively.

The inverse τ_K matrices, τ_K^{-1}, for $K = 2, 3, 4$, which are used in this work, are given explicitly below:

$$\tau_2^{-1} = \frac{1}{2} \begin{pmatrix} 1 & -1 \\ 1 & 1 \end{pmatrix}, \quad \tau_3^{-1} = \frac{1}{3} \begin{pmatrix} 1 & -2 & 0 \\ 1 & 1 & -\sqrt{3} \\ 1 & 1 & \sqrt{3} \end{pmatrix},$$

$$\tau_4^{-1} = \frac{1}{4} \begin{pmatrix} 1 & -2 & 0 & -1 \\ 1 & 0 & -2 & 1 \\ 1 & 2 & 0 & -1 \\ 1 & 0 & 2 & 1 \end{pmatrix}. \tag{A4}$$

For triplet or three-body, the probability function is expressed in a manner similar to Eq. (11).

$$y_{3,n}^{ABC} = \sum_s \left(\tau_K^{-1} \otimes \tau_K^{-1} \otimes \tau_K^{-1} \right)_{ABC,(s)} \left\langle \Gamma_{3,n}^{(s)} \right\rangle. \tag{A5}$$

For four-body, the probability expression reads:

$$y_{4,n}^{ABCD} = \sum_s \left(\tau_K^{-1} \otimes \tau_K^{-1} \otimes \tau_K^{-1} \otimes \tau_K^{-1} \right)_{ABCD,(s)} \left\langle \Gamma_{4,n}^{(s)} \right\rangle. \tag{A6}$$

Warren-Cowley SRO parameters are computed via the point and pair correlation functions. For a quaternary system, the analytical formulas for SRO parameters are as follows:

$$\alpha_n^{AB} = \alpha_n^{\text{Cr-Fe}} = 1 - \frac{1 - 2\left(\left\langle \Gamma_{1,1}^1 \right\rangle + \left\langle \Gamma_{1,1}^2 \right\rangle - 2\left\langle \Gamma_{2,n}^{12} \right\rangle + \left\langle \Gamma_{2,n}^{13} \right\rangle - \left\langle \Gamma_{2,n}^{23} \right\rangle\right) - \left\langle \Gamma_{2,n}^{33} \right\rangle}{\left(1 - 2\left\langle \Gamma_{1,1}^1 \right\rangle - \left\langle \Gamma_{1,1}^3 \right\rangle\right)\left(1 - 2\left\langle \Gamma_{1,1}^2 \right\rangle + \left\langle \Gamma_{1,1}^3 \right\rangle\right)}$$

$$\alpha_n^{AC} = \alpha_n^{\text{Cr-Mn}} = 1 - \frac{1 - 2\left\langle \Gamma_{1,1}^3 \right\rangle - 4\left\langle \Gamma_{2,n}^{11} \right\rangle + \left\langle \Gamma_{2,n}^{33} \right\rangle}{-4\left\langle \Gamma_{1,1}^1 \right\rangle^2 + \left(1 - \left\langle \Gamma_{1,1}^3 \right\rangle\right)^2}$$

$$\alpha_n^{AD} = \alpha_n^{\text{Cr-Ni}} = 1 - \frac{1 - 2\big(\langle\Gamma_{1,1}^1\rangle - \langle\Gamma_{1,1}^2\rangle + 2\langle\Gamma_{2,n}^{12}\rangle + \langle\Gamma_{2,n}^{13}\rangle + \langle\Gamma_{2,n}^{23}\rangle\big) - \langle\Gamma_{2,n}^{33}\rangle}{\big(1 - 2\langle\Gamma_{1,1}^1\rangle - \langle\Gamma_{1,1}^3\rangle\big)\big(1 + 2\langle\Gamma_{1,1}^2\rangle + \langle\Gamma_{1,1}^3\rangle\big)} \tag{A7}$$

$$\alpha_n^{BC} = \alpha_n^{\text{Fe-Mn}} = 1 - \frac{1 + 2\big(\langle\Gamma_{1,1}^1\rangle - \langle\Gamma_{1,1}^2\rangle - 2\langle\Gamma_{2,n}^{12}\rangle + \langle\Gamma_{2,n}^{13}\rangle + \langle\Gamma_{2,n}^{23}\rangle\big) - \langle\Gamma_{2,n}^{33}\rangle}{\big(1 + 2\langle\Gamma_{1,1}^1\rangle - \langle\Gamma_{1,1}^3\rangle\big)\big(1 - 2\langle\Gamma_{1,1}^2\rangle + \langle\Gamma_{1,1}^3\rangle\big)}$$

$$\alpha_n^{BD} = \alpha_n^{\text{Fe-Ni}} = 1 - \frac{1 + 2\langle\Gamma_{1,1}^3\rangle - 4\langle\Gamma_{2,n}^{22}\rangle + \langle\Gamma_{2,n}^{33}\rangle}{-4\langle\Gamma_{1,1}^2\rangle^2 + \big(1 + \langle\Gamma_{1,1}^3\rangle\big)^2}$$

$$\alpha_n^{CD} = \alpha_n^{\text{Mn-Ni}} = 1 - \frac{1 + 2\big(\langle\Gamma_{1,1}^1\rangle + \langle\Gamma_{1,1}^2\rangle + 2\langle\Gamma_{2,n}^{12}\rangle + \langle\Gamma_{2,n}^{13}\rangle - \langle\Gamma_{2,n}^{23}\rangle\big) - \langle\Gamma_{2,n}^{33}\rangle}{\big(1 + 2\langle\Gamma_{1,1}^1\rangle - \langle\Gamma_{1,1}^3\rangle\big)\big(1 + 2\langle\Gamma_{1,1}^2\rangle + \langle\Gamma_{1,1}^3\rangle\big)}$$

APPENDIX B: DFT CALCULATIONS OF PURE MN

Binding energy curves for different Mn structures are shown in Fig. 18 with a reference to the binding energy of α-Mn GS ($E - E_{\alpha\text{-Mn}}^{\text{AFM}}$). It can be seen from Fig. 18, that lowering the volume per atoms significantly below the equilibrium volume for each structure leads the magnetic ordering to change to the nonmagnetic, indicating the high-pressure magnetic phase transition. The comparison of magnetic ordering, volume per atom and the $E - E_{\alpha\text{-Mn}}^{\text{AFM}}$ values with experimental and theoretical results are presented in Table IV. Magneto-volume relation for studied structural and magnetic phases of Mn with nonzero AMMM is presented in Fig. 19(a) and

it shows that the volume per atom increases with increasing AMMM in all structures.

The GS of Mn, α-Mn, has a very complex atomic structure. The lattice is identified as σ-phase with 58 atoms in the unit cell and four crystallographically and magnetically inequivalent sites, where the half of the atoms in each site is ordered antiferromagnetically to the other half. Table V presents the comparison of the magnitudes of magnetic moments for these sites with the previous experimental and theoretical results. It can be seen that the values obtained in this work lie within the range of previous experimental and theoretical results. Magneto-volume relation for each site is shown in Fig. 19(b).

APPENDIX C: BINARY SUBSYSTEMS WITHOUT MN

In addition to the results of Wróbel *et al.* [22] for Fe-Cr, Cr-Ni, and Fe-Ni binaries, SQSs in these subsystems have been included into consideration. Formation enthalpies, volumes per atom and average magnitudes of magnetic moments of SQSs have been calculated and compared to those of the ordered structures.

1. Fe-Cr binary

Ground states in terms of mixing enthalpy are FeCr$_5$, FeCr$_2$ [β_2(100)], Fe$_3$Cr$_5$, FeCr (L1$_0$), Fe$_3$Cr (L1$_2$). Previously predicted GS FeCr$_8$ [22] lies within the convex hull with the addition of predicted FeCr$_5$ alloy. Fe$_3$Cr$_5$ intermetallic lies almost exactly on the convex hull line and may not be GS in terms of H_{mix} [see Fig. 20(a)].

All of the structures show positie values of the formation enthalpy which can be interpreted as metastability and hence the transformation to α and σ phases [22,136] may be more preferable. Stability regions of magnetic structures [see Fig. 20(c)] are divided with FM FeCr$_2$ structure with 66.(6) at. % Cr—smaller Cr concentration results in domination of magnetic moments of Fe with FiM ordering, which is consistent with previous calculations [137], and larger Cr concentration suppresses the magnetism of Fe and yields NM ordering. Total magnetic moment of the system grows with the increasing Fe concentration in the FiM region. Atomic volumes of Fe-Cr alloys in NM region are underestimated compared to Vegard's law for NM reference structures within

FIG. 18. Calculated equations of state for known and hypothetical crystal structures and magnetic configurations of Mn.

TABLE IV. Magnetic ordering, AMMM (in μ_B), volume per atom (in Å^3) and $E - E_{\alpha\text{-Mn}}^{\text{AFM}}$ (in meV) for different phases of pure Mn compared to previous experimental and theoretical data.

Phase	Magnetic ordering		AMMM (μ_B)			V/at (Å^3)			$E - E_{\alpha\text{-Mn}}^{\text{AFM}}$ (meV)	
	Prev.	Present	Theor.	Exp.	Present	Theor.	Exp.	Present	Prev.	Present
α-Mn	AFM	NM			0	10.75[a]		10.74		21
		AFM		0.5[b]	0.57	11.08[c]	12.05[d]	11.13	0[c]	0
β-Mn	FiM	NM			0	12.17[e]		10.81		72
		AFM	0.5[e]		0.24	12.40[e], 10.84[c]	12.44[e,f,g]	10.82	63[c]	71
γ-Mn (fcc)	AFM	NM			0			10.67		102
		AFMSL	2.13[h]		1.84	11.16[c]	12.95[i]	11.37	67[c]	52
		AFMDL			1.28			11.02		94
		AFMQL			1.14			10.98		93
δ-Mn (bcc)	AFM	NM			0			10.70		185
		FM	0.99[h]		0.85	11.12[c]		10.86	146[c]	167
		AFMDL			0.54			10.77		181
		AFMTL			0.98			10.97		157
		AFMQL			0.78			10.95		158
ϵ-Mn (hcp)	AFM	NM			0			10.63		72
		AFM	0.20[h]		0.53	10.72[c]		10.69	61[c]	70

[a]Hobbs *et al.* [73].
[b]Shull and Wilkinson [129].
[c]Hafner and Hobbs [130].
[d]Lawson *et al.* [70].
[e]Asada [131].
[f]Preston [132].
[g]Sliwko *et al.* [133].
[h]Asada and Terakura [134].
[i]Wyckoff [135].

0.1 Å^3 per atom [see Fig. 20(b)]. Volumes derived from Vegard's law for magnetic structures are higher than those for NM structures, and the structures in FiM region lie between the two. Evaluated average magnitudes of magnetic moments are underestimated compared to experimental results [138] by 0.2 μ_B at least up to 16 at. % Cr. Values of H_{form}, volumes per atom and AMMM of SQSs have continuous behavior and converge to the values of NM Cr and FM Fe in the corresponding ends of the concentration scale. Magnetic order of SQSs is FiM up to 75 at. % Cr, even for the concentrations close to NM Cr$_2$Fe.

2. Fe-Ni binary

Ground states in terms of enthalpy of mixing are FeNi$_3$ (L1$_2$), FeNi$_8$ (Pt$_8$Ti-like), FeNi (L1$_0$), Fe$_3$Ni$_2$ (I4/mmm-symmetry), and FeNi$_5$. All GSs except FeNi$_5$ are consistent with previous calculations [22] and the latter lies almost on convex hull line [see Fig. 21(a)]. In terms of formation enthalpy GSs are located only in Ni-rich region, which are FeNi and FeNi$_3$, observed experimentally in Ref. [139] and FeNi$_8$, previously preicted in Ref. [140]. This can be due to the fact that Ni is the fcc stabilizer and VEC for FeNi already
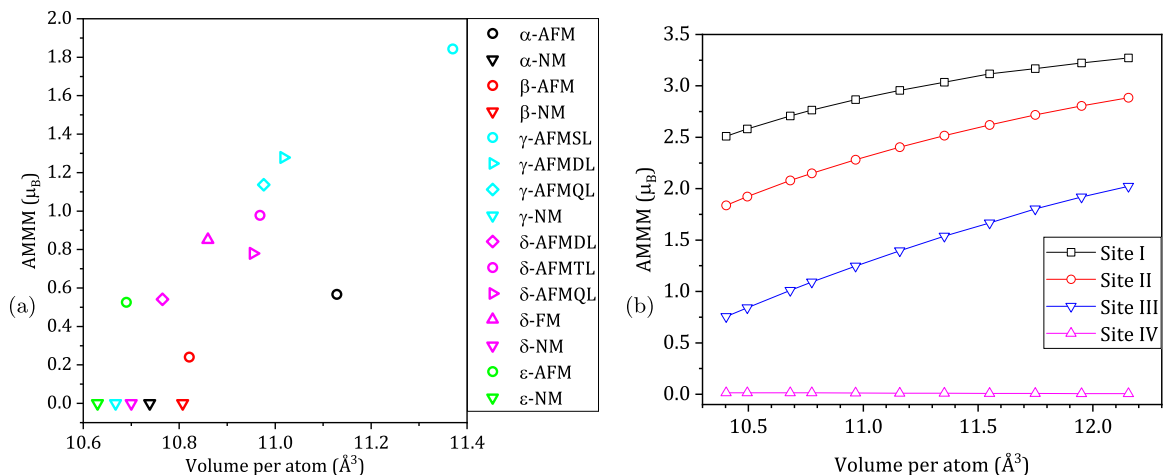

FIG. 19. Magneto-volume relation (a) for all calculated Mn structures at equilibrium volume and (b) for four sites in AFM α-Mn.

TABLE V. AMMM (in μ_B) of atoms on different sites in AFM α-Mn structure compared to previous experimental and theoretical data.

Site	No. of atoms	Expt.[a] Col.	Expt.[b] Col.	Expt.[c] Col.1	Expt.[c] Col.2	Expt.[d] N.Col.	Expt.[e] N.Col.	Expt.[f] N.Col.1	Expt.[f] N.Col.2	Theor.[g] Col.1	Theor.[g] Col.2	Present work
						AMMM (μ_B)						
I	2	1.35	1.8	1.54	2.5	2.83	2.05	2.05	1.9	2.79	3.19	2.94
II	8	1.35	1.4	1.54	2.5	1.83	1.80	1.79	1.7	2.22	2.79	2.39
III	24	0.99	1.2	3.08	1.7	0.61	0.60	0.59	0.6	1.11	1.81	1.38
IV	24	0.22	0.1	0	0	0.47	0.27	0.27	0.2	0.07	0	0.02

[a]Kunitomi *et al.* [67].
[b]Oberteuffer *et al.* [68].
[c]Kasper and Roberts [69]; models 1 and 2 represent different fits to the same set of diffraction data.
[d]Lawson *et al.* [70].
[e]Yamagata and Tazawa [71].
[f]Yamada *et al.* [72]; models 1 and 2 are based on different choices of the magnetic form factor.
[g]Hobbs *et al.* [73]; calculations 1 and 2 have been done for different volumes per atom: 11.23 $\mathring{A}^3$ and 12.05 $\mathring{A}^3$, respectively.

exceeds the required fcc stability threshold. Values of H_{form} of SQSs have continuous behavior between FM Fe and FM Ni.

Regions of stability for different magnetic configurations [see Fig. 21(c)] are divided by the FM Fe$_3$Ni$_2$ structure at 40% of Ni concentration—the most stable structures with higher Ni concentration have FM ordering and the most stable structures with lower Ni concentration have FiM ordering. The Vegard's law estimate of the volume per atom for magnetic reference structures drops with Ni concentration and yields higher values than the estimate for nonmagnetic reference structures, which moreover increases with increasing Ni concentration [see Fig. 21(b)]. The values of the volumes per atom from the current calculations are overestimated compared to the

magnetic estimate with maximum difference of 0.4 $\mathring{A}^3$ per atom, and linear behavior of volume per atom as a function of Ni concentration holds only in the FM region. Values of magnetic moments for individual elements grow with the increasing Ni concentration, and the values of total magnetic moments decrease with the increasing Ni concentration, showing almost linear dependency. The values of magnetic moments, volumes per atom and enthalpies of mixing are

FIG. 21. Enthalpy of formation, volume per atom and magnetic moments per atom for stable states calculated using DFT for Fe-Ni alloys on fcc lattice. The notation is the same as in Fig. 2. Black dash-dotted line connects the true GSs, which are FM bcc Fe and FM fcc Ni. Experimental data: [a]Reck *et al.* [121], [b]Shull *et al.* [93], [c]Cochrane *et al.* [142], [d]Nakai *et al.* [143], [e]Menshikov *et al.* [144], [f]Wakelin *et al.* [122], [g]Owen *et al.* [120], [h]Bhatia *et al.* [123], [i]Shiga [145], [j]Chamberod *et al.* [146].
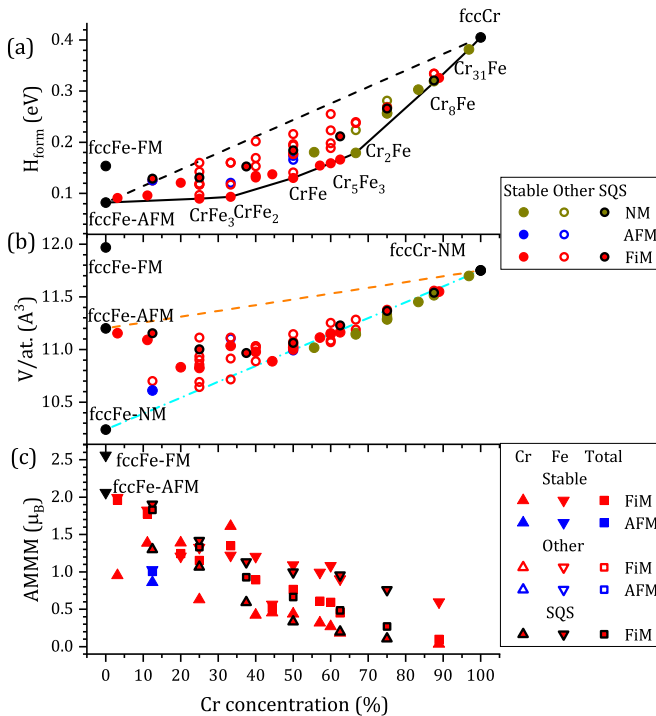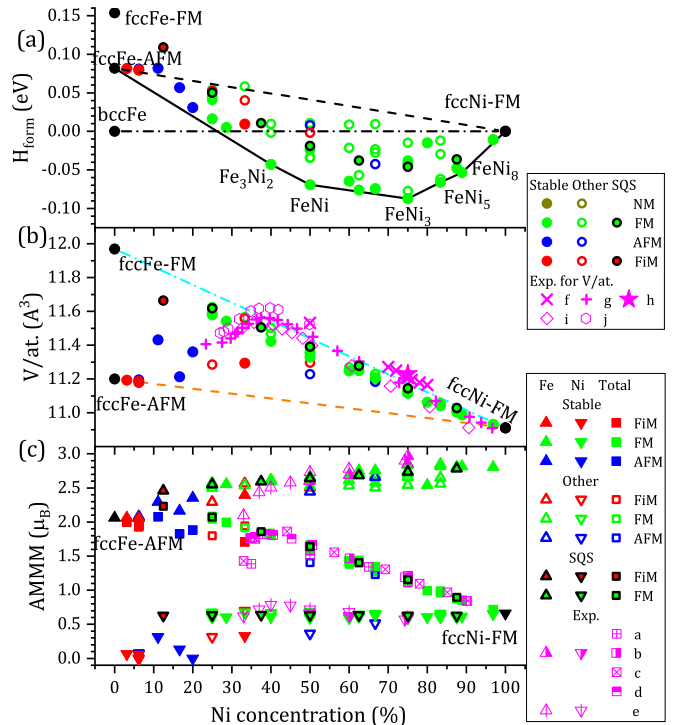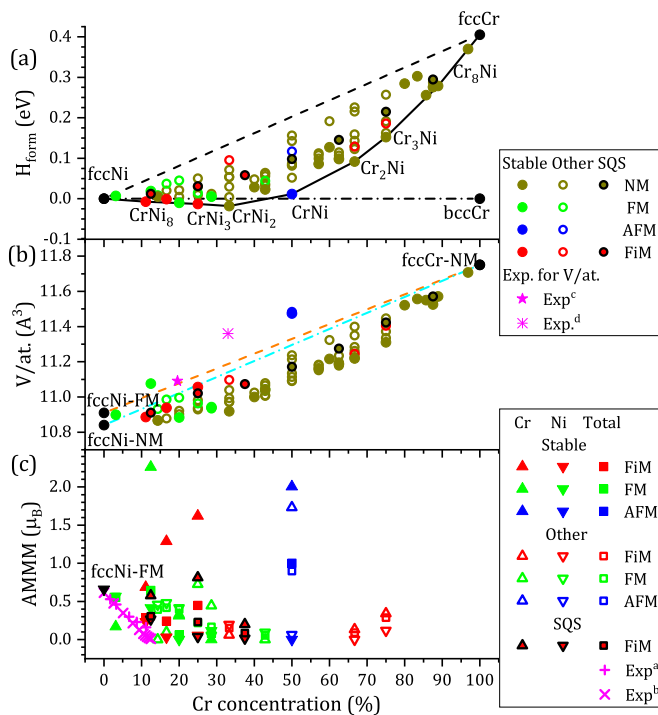

FIG. 20. (a) Enthalpy of formation, (b) average magnitudes of magnetic moments per atom, (c) volume per atom of fcc Cr-Fe structures calculated using DFT. The notation is the same as in Fig. 2.

FIG. 22. Enthalpy of formation, volume per atom and magnetic moments per atom for stable states calculated using DFT for Cr-Ni alloys on fcc lattice. The notation is the same as in Fig. 2. Black dash-dotted line connects the true GSs, which are FM fcc Ni and AFM bcc Cr. Experimental data are taken from: [a]Takano *et al.* [119], [b]Besnus *et al.* [147], [c]Lenkkeri [148], [d]Jung [118].

in agreement with experimental data [139]. Our results for the average magnetic moment values correspond to the data from Ref. [141] observed for coexisting fcc and bcc phases. Magnetic stability of SQSs corresponds to the stability of ordered structures—SQS with 12.5 at. % Ni is FiM and all SQS with higher Ni concentration are FM.

Values of volumes per atom and AMMM of FM SQS structures (25–87.5 at. % Ni) closely correspond to the values

for calculated ordered structures and at the 37.5–87.5 at. % Ni concentrations have a good correspondence with the experimental data from Refs. [139,141].

3. Cr-Ni binary

Ground states in terms of mixing enthalpy are Cr_8Ni ($NbNi_8$-like), Cr_3Ni (Z1(100)), Cr_2Ni (β1(100)), CrNi ($L1_1$), $CrNi_2$, $CrNi_3$ [Y3(110)]. Contrary to the previous predictions [22], the current study shows that Cr_7Ni and Cr_5Ni lie inside the convex hull due to the presence of Cr_8Ni [see Fig. 22(a)]. In terms of formation enthalpy, only $CrNi_2$ which is located in the Ni-rich region is considered to be a stable state. Values of H_{form} of SQSs have continuous behavior between FM Ni and NM Cr.

The Stability regions of different magnetic configuration [see Fig. 22(c)] are divided with FiM CrNi and the structures with higher Cr content are NM. Magnetic ordering in the region of Cr concentrations below 50% is not clear, because the magnetic ordering of pure Ni is FM, but the most stable structures (which are most close to the convex hull) in this region have different magnetic ordering. Stable FiM structures in this region show peculiar behavior compared to other binaries—values of Cr magnetic moments grow with the increasing Cr concentration up to 50% Cr and reach the value of 2 μ_B, having a higher impact on the total magnetic moment, though GS and the most stable fcc state of the pure Cr is NM. Magnetic ordering of SQSs in the region of NM stability of ordered structures is also NM, but in the region of concentrations below 50 at. % Cr, where ordered FiM and FM structures are the most stable, SQSs possess only FiM ordering.

The maximum difference between the Vegard's law estimate for the magnetic and the NM reference structures is 0.1 Å^3 and the values of volumes per atom are underestimated up to 0.3 Å^3 [see Fig. 22(b)]. Values of volumes per atom for SQSs are lower compared to the NM Vegard's law estimate with a maximum difference of 0.1 Å^3, similarly to ordered structures.

[1] B. Cantor, I. T. H. Chang, P. Knight, and A. J. B. Vincent, Mat. Sci. Eng. A **375-377**, 213 (2004).

[2] A. S. Sharma, S. Yadav, K. Biswas, and B. Basu, Mater. Sci. Eng. R **131**, 1 (2018).

[3] D. B. Miracle and O. N. Senkov, Acta Mater. **122**, 448 (2017).

[4] B. J.-w. Yeh, S.-k. Chen, J.-y. Lin, Su-jien Gan, T.-s. Chin, T.-t. Shun, and C.-h. Tsau, Adv. Eng. Mater. **6**, 299 (2004).

[5] Y. Zhang, S. Guo, C. T. Liu, and X. Yang, *High-Entropy Alloys. Fundamentals and Application* (Springer, Cham, 2016), p. 516.

[6] H. S. Oh, D. Ma, G. P. Leyson, B. Grabowski, E. S. Park, F. Körmann, and D. Raabe, Entropy **18**, 321 (2016).

[7] Z. Li, S. Zhao, R. O. Ritchie, and M. A. Meyers, Prog. Mater. Sci. **102**, 296 (2018).

[8] O. El-Atwani, N. Li, M. Li, A. Devaraj, J. K. S. Baldwin, M. M. Schneider, D. Sobieraj, J. S. Wróbel, D. Nguyen-Manh,

S. A. Maloy, and E. Martinez, Sci. Adv. **5**, eaav2002 (2019).

[9] N. K. Kumar, C. Li, K. Leonard, H. Bei, and S. Zinkle, Acta Mater. **113**, 230 (2016).

[10] K. Jin, C. Lu, L. Wang, J. Qu, W. Weber, Y. Zhang, and H. Bei, Scr. Mater. **119**, 65 (2016).

[11] C. Lu, L. Niu, N. Chen, K. Jin, T. Yang, P. Xiu, Y. Zhang, F. Gao, H. Bei, S. Shi, M. R. He, I. M. Robertson, W. J. Weber, and L. Wang, Nat. Commun. **7**, 13564 (2016).

[12] C. Li, J. Yin, K. Odbadrakh, B. C. Sales, S. J. Zinkle, G. M. Stocks, and B. D. Wirth, J. Appl. Phys. **125**, 155103 (2019).

[13] S. Guo, C. Ng, J. Lu, and C. T. Liu, J. Appl. Phys. **109**, 103505 (2011).

[14] Z. Leong, J. S. Wróbel, S. L. Dudarev, R. Goodall, I. Todd, and D. Nguyen-Manh, Sci. Rep. **7**, 39803 (2017).

[15] Y. Ikeda, B. Grabowski, and F. Körmann, Mater. Charact. **147**, 464 (2019).

[16] Z. Wu and H. Bei, Mat. Sci. Eng. A **640**, 217 (2015).

[17] N. D. Stepanov, D. G. Shaysultanov, M. A. Tikhonovsky, and G. A. Salishchev, Mater. Des. **87**, 60 (2015).

[18] E. J. Pickering, R. Muñoz-Moreno, H. J. Stone, and N. G. Jones, Scr. Mater. **113**, 106 (2016).

[19] N. D. Stepanov, D. G. Shaysultanov, M. S. Ozerov, S. V. Zherebtsov, and G. A. Salishchev, Mater. Lett. **185**, 1 (2016).

[20] F. Otto, A. Dlouhý, K. G. Pradeep, M. Kuběnová, D. Raabe, G. Eggeler, and E. P. George, Acta Mater. **112**, 40 (2016).

[21] G. Bracq, M. Laurent-brocq, L. Perri, J.-M. Joubert, and I. Guillot, Acta Mater. **128**, 327 (2017).

[22] J. S. Wróbel, D. Nguyen-Manh, M. Y. Lavrentiev, M. Muzyk, and S. L. Dudarev, Phys. Rev. B **91**, 024108 (2015).

[23] R. Martin, *Electronic Structure: Basic Theory and Practical Methods* (Cambridbe University Press, Cambridge, 2004), p. 650.

[24] L. Piela, *Ideas of Quantum Chemistry* (Elsevier, Amsterdam, 2013), p. 1078.

[25] J. Hafner, J. Comput. Chem. **29**, 2044 (2008).

[26] E. Engel and D. M. Reiner, *Density Functional Theory: An Advanced Course* (Springer-Verlag, Berlin, 2011), p. 531.

[27] P. J. Hasnip, K. Refson, M. I. J. Probert, J. R. Yates, S. J. Clark, and C. J. Pickard, Philos. Trans. Royal Soc. A **372**, 20130270 (2014).

[28] J. M. Sanchez, Physica A **128**, 334 (1984).

[29] J. W. D. Connolly and A. R. Williams, Phys. Rev. B **27**, 5169 (1983).

[30] J. M. Sanchez, Phys. Rev. B **81**, 224202 (2010).

[31] A. V. Ruban and I. A. Abrikosov, Rep. Prog. Phys. **71**, 046501 (2008).

[32] S. N. Khan, J. B. Staunton, and G. M. Stocks, Phys. Rev. B **93**, 054206 (2016).

[33] P. Singh, A. V. Smirnov, and D. D. Johnson, Phys. Rev. B **91**, 224204 (2015).

[34] A. van de Walle and G. Ceder, J. Phase Equilib. **23**, 348 (2002).

[35] A. Fernández-Caballero, M. Fedorov, J. S. Wróbel, P. M. Mummery, and D. Nguyen-Manh, Entropy **21**, 68 (2019).

[36] A. van de Walle, Calphad **33**, 266 (2009).

[37] A. Fernández-Caballero, J. S. Wróbel, P. M. Mummery, and D. Nguyen-Manh, J. Phase Equilib. Diff. **38**, 391 (2017).

[38] J. A. Barker, Proc. R. Soc. Lond. A **216**, 45 (1952).

[39] See Supplemental Material at http://link.aps.org/supplemental/10.1103/PhysRevB.101.174416 for additional information not fit for the main part of the manuscript, including the results from DFT, intermediate data from Cluster Expansion, and the analysis of short-range order for Ni$_x$[CrFeMn]$_{1-x}$ pseudobinaries.

[40] B. Fultz, Prog. Mater. Sci. **55**, 247 (2010).

[41] C. Wolverton and A. Zunger, Phys. Rev. B **52**, 8813 (1995).

[42] G. Grimvall, *Thermophysical Properties of Materials* (Elsevier Science, Amsterdam, 1999), p. 424.

[43] M. Y. Lavrentiev, D. Nguyen-Manh, and S. L. Dudarev, Phys. Rev. B **81**, 184202 (2010).

[44] F. Körmann, Y. Ikeda, B. Grabowski, and M. H. Sluiter, npj Comput. Mater. **3**, 36 (2017).

[45] D. Ma, B. Grabowski, F. Körmann, J. Neugebauer, and D. Raabe, Acta Mater. **100**, 90 (2015).

[46] K. Jin, B. C. Sales, G. M. Stocks, G. D. Samolyuk, M. Daene, W. J. Weber, and Y. Zhang, Sci. Rep. **6**, 20159 (2016).

[47] S. Mu, Z. Pei, X. Liu, and G. M. Stocks, J. Mater. Res. **33**, 2857 (2018).

[48] M. Y. Lavrentiev, J. S. Wróbel, D. Nguyen-Manh, S. L. Dudarev, and M. G. Ganchenkova, J. Appl. Phys. **120**, 043902 (2016).

[49] I. Toda-Caraballo, J. S. Wróbel, D. Nguyen-Manh, P. Pérez, and P. E. J. Rivera-Díaz-del Castillo, JOM **69**, 2137 (2017).

[50] A. van de Walle and G. Ceder, Rev. Mod. Phys. **74**, 11 (2002).

[51] G. Kresse and J. Hafner, Phys. Rev. B **47**, 558 (1993).

[52] G. Kresse and J. Hafner, Phys. Rev. B **49**, 14251 (1994).

[53] G. Kresse and J. Furthmüller, Comput. Mater. Sci. **6**, 15 (1996).

[54] G. Kresse and J. Furthmüller, Phys. Rev. B **54**, 11169 (1996).

[55] P. E. Blöchl, Phys. Rev. B **50**, 17953 (1994).

[56] G. Kresse and D. Joubert, Phys. Rev. B **59**, 1758 (1999).

[57] J. P. Perdew, K. Burke, and M. Ernzerhof, Phys. Rev. Lett. **77**, 3865 (1996).

[58] J. D. Pack and H. J. Monkhorst, Phys. Rev. B **13**, 5188 (1976).

[59] A. van de Walle, P. Tiwary, M. de Jong, D. L. Olmsted, M. Asta, A. Dick, D. Shin, Y. Wang, L.-Q. Chen, and Z.-K. Liu, Calphad **42**, 13 (2013).

[60] A. van de Walle and M. Asta, Model. Simul. Mater. Sci. Eng. A **10**, 521 (2002).

[61] G. L. W. Hart and R. W. Forcade, Phys. Rev. B **77**, 224115 (2008).

[62] S. V. Barabash, V. Blum, S. Müller, and A. Zunger, Phys. Rev. B **74**, 035108 (2006).

[63] G. Ceder, G. D. Garbulsky, D. Avis, and K. Fukuda, Phys. Rev. B **49**, 1 (1994).

[64] N. A. Zarkevich and D. D. Johnson, Phys. Rev. Lett. **92**, 255702 (2004).

[65] E. Wohlfarth, *Handbook of Ferromagnetic Materials*, Vol. 1 (Elsevier B.V., Amsterdam, 1980), pp. 1–70.

[66] M. Steinitz, J. Magn. Magn. Mater. **60**, 137 (1986).

[67] N. Kunitomi, T. Yamada, Y. Nakai, and Y. Fujii, J. Appl. Phys. **40**, 1265 (1969).

[68] J. A. Oberteuffer, J. A. Marcus, L. H. Schwartz, and G. P. Felcher, Phys. Lett. **28**, 267 (1968).

[69] J. Kasper and B. Roberts, Phys. Rev. **101**, 537 (1956).

[70] A. C. Lawson, A. C. Larson, M. C. Aronson, S. Johnson, Z. Fisk, P. C. Canfield, J. D. Thompson, and R. B. Von Dreele, J. Appl. Phys. **76**, 7049 (1994).

[71] H. Yamagata and K. Asayama, J. Phys. Soc. Jpn. **33**, 400 (1972).

[72] T. Yamada, N. Kunitomi, and Y. Nakai, J. Phys. Soc. Jpn. **28**, 615 (1970).

[73] D. Hobbs, J. Hafner, and D. Spišák, Phys. Rev. B **68**, 014407 (2003).

[74] V. T. Witusiewicz, F. Sommer, and E. J. Mittemeijer, J. Phase Equilib. Diff. **25**, 346 (2004).

[75] S. Lintzen, J. von Appen, B. Hallstedt, and R. Dronskowski, J. Alloys Compd. **577**, 370 (2013).

[76] V. T. Witusiewicz, F. Sommer, and E. J. Mittemeijer, Metall. Mater. Trans. B **34**, 209 (2003).

[77] Y. Yang, Z. Shen, L. Liu, Y. Zhang, C. Song, and Q. Zhai, Mat. Res. **18**(Suppl. 1), 10 (2015).

[78] J. Chen and W.-n. Zhang, Mater. Sci. Tech. **34**, 63 (2018).

[79] X. Liang, Structure and Mechanical Properties of Fe-Mn Alloys, Master's thesis, McMaster University, 2008.

[80] S. Ruiz-Gómez, R. Ranchal, M. Abuín, A. M. Aragón, V. Velasco, P. Marín, A. Mascaraque, and L. Pérez, Phys. Chem. Chem. Phys. **18**, 8212 (2016).

[81] Y. Ishikawa and Y. Endoh, J. Appl. Phys. **39**, 1318 (1968).

[82] C. Kimball, W. D. Gerber, and A. Arrott, J. Appl. Phys. **34**, 1046 (1963).

[83] R. Kubitz and F. H. Hayes, Monatsh. Chem. **118**, 31 (1987).

[84] M. Huang, P. F. Ladwig, and Y. Austin Chang, Thin Solid Films **478**, 137 (2005).

[85] V. G. Pushin, N. N. Kuranova, E. B. Marchenkova, E. S. Belosludtseva, V. A. Kazantsev, and N. I. Kourov, Tech. Phys. **58**, 878 (2013).

[86] C. Guo and Z. Du, Intermetallics **13**, 525 (2005).

[87] N. A. Gokcen, J. Phase Equilib. **12**, 313 (1991).

[88] N. Honda, Y. Tanji, and Y. Nakagawa, J. Phys. Soc. Jpn. **41**, 1931 (1976).

[89] W. B. Pearson, K. Brun, and A. Kjerkshus, Acta Chem. Scand. **19**, 477 (1965).

[90] E. Krén, E. Nagy, I. Nagy, L. Pál, and P. Szabó, J. Phys. Chem. Solids **29**, 101 (1968).

[91] C. Petrillo, F. Sacchetti, and M. Scafi, J. Magn. Magn. Mater. **104–107**, 2015 (1992).

[92] A. Paoletti and F. P. Ricci, J. Appl. Phys. **34**, 1571 (1963).

[93] C. G. Shull and M. K. Wilkinson, Phys. Rev. **97**, 304 (1955).

[94] F. Kajzar and A. Delapalme, J. Magn. Magn. Mater. **14**, 139 (1979).

[95] J. S. Kasper and J. S. Kouvel, J. Phys. Chem. Solids **11**, 231 (1959).

[96] J. Cable and Y. Tsunoda, J. Magn. Magn. Mater. **140-144**, 93 (1995).

[97] D. Spisák and J. Hafner, J. Phys. Condens. Matter **11**, 6359 (1999).

[98] H. Tange, T. Tokunaga, and M. Goto, J. Phys. Soc. Jpn. **45**, 105 (1978).

[99] B. Shanina and V. G. Gavriljuk, Mater. Sci. Forum **638-642**, 3015 (2010).

[100] M. Takahashi, A. Kumar Das, T. Sembiring, H. Iwasaki, and K. Ohshima, Physica B **385-386**, 130 (2006).

[101] M. Takahashi, E. Ahmed, A. Kumar, and Y. Fujii, J. Alloys Compd. **453**, 75 (2008).

[102] A. B. Ziya, M. Takahashi, and K. Ohshima, J. Alloys Compd. **479**, 60 (2009).

[103] H. Sugimura, Y. Kaneno, and T. Takasugi, Mater. Trans. **52**, 1569 (2011).

[104] J. Vrestál, CrFeMn iron systems, in *Landolt-Börnstein—Group iv Physical Chemistry*, Part 4 (Springer-Verlag, Berlin, 2008).

[105] Y. Matsumot and K. Koyama, ISIJ Int. **30**, 927 (1990).

[106] J. S. Kouvel, J. Phys. Chem. Solids **16**, 152 (1960).

[107] J. S. Kouvel and J. S. Kasper, J. Phys. Chem. Solids **24**, 529 (1963).

[108] J. Singh and C. Wayman, Mater. Sci. Eng. **94**, 233 (1987).

[109] Y.-U. Heo, M. Kim, and H.-C. Lee, Acta Mater. **56**, 1306 (2008).

[110] A. Z. Menshikov, V. A. Kazantsev, and N. N. Kuzmin, Pisma Zh. Eksp. Teor. Fiz. **23**, 6 (1976) [Sov. Phys. JETP Lett. **23**, 6 (1976)].

[111] E. F. Wassermann, Phys. Scr. **T25**, 209 (1989).

[112] H. H. Ettwig and W. Pepperhoff, Phys. Status Solidi A **23**, 105 (1974).

[113] A. Menshikov, P. Burlet, A. Chamberod, and J. Tholence, Solid State Commun. **39**, 1093 (1981).

[114] T. Shimura and A. I. S. Kemp, Am. Mineral. **100**, 2545 (2015).

[115] C. Cucciniello, Periodico di Mineralogia **85**, 115 (2016).

[116] S. Hossein Nedjad, S. Meimandi, A. Mahmoudi, T. Abedi, S. Yazdani, H. Shirazi, and M. Nili Ahmadabadi, Mater. Sci. Eng. A **501**, 182 (2009).

[117] D. Geissler, K. H. Müller, J. Freudenberger, K. Nenkov, M. Krautz, J. Eickemeyer, and L. Schultz, J. Alloys Compd. **509**, 3726 (2011).

[118] P. Ehrhart, P. Jung, H. Schultz, and H. Ullmaier, *Atomic Defects in Metals*, Vol. III/25 (Springer-Verlag, Berlin, 1991), p. 437.

[119] Y. Takano and S. Chikazumi, Kobayashi Rigaku Kenkyusho Hokoku **9**, 12 (1959); H. P. J. Wijn (ed.), *Magnetic Properties of Metals, Landolt-Börstein*, Numerical Data and Functional Relationships in Science and Technology, Vol. 19 (Springer, Berlin, Heidelberg, 1991).

[120] E. A. Owen, E. L. Yates, and A. H. Sully, Proc. Phys. Soc. **49**, 315 (1937).

[121] R. A. Reck and D. L. Fry, Phys. Rev. **184**, 492 (1969).

[122] R. J. Wakelin and E. L. Yates, Proc. Phys. Soc. **66**, 221 (1953).

[123] M. L. Bhatia, A. K. Singh, and T. K. Nandy, Intermetallics **4**, 635 (1996).

[124] M. Lavrentiev, S. L. Dudarev, and D. Nguyen-Manh, J. Nucl. Mater. **386-388**, 22 (2009).

[125] M. E. J. Newman and G. T. Barkema, *Monte Carlo Methods in Statistical Physics* (Clarendon Press, London, 1999), p. 490.

[126] G. Federici, W. Biel, M. R. Gilbert, R. Kemp, N. Taylor, and R. Wenninger, Nucl. Fus. **57**, 092002 (2017).

[127] P. Cenedese, F. Bley, and S. Lefebvre, Acta Crystallogr. A **40**, 228 (1984).

[128] A. Z. Menshikov, C. Dimitrov, and A. E. Teplykh, J. Phys. III France **7**, 1899 (1997).

[129] C. G. Shull and M. K. Wilkinson, Rev. Mod. Phys. **25**, 100 (1953).

[130] J. Hafner and D. Hobbs, Phys. Rev. B **68**, 014408 (2003).

[131] T. Asada, J. Magn. Magn. Mater. **140-144**, 47 (1995).

[132] G. D. Preston, Philos. Mag. **5**, 1207 (1928).

[133] V. Sliwko, P. Mohn, and K. Schwarz, J. Phys. Condens. Matter **6**, 6557 (1994).

[134] T. Asada and K. Terakura, Phys. Rev. B **47**, 15992 (1993).

[135] R. W. G. Wyckoff (ed.), *Crystal Structure* (Wiley, New York, 1963).

[136] M. S. Dubiel and J. Cieslak, Crit. Rev. Solid State **36**, 191 (2011).

[137] D. Nguyen-Manh, P. W. Ma, M. Y. Lavrentiev, and S. L. Dudarev, Ann. Nucl. Energy **77**, 246 (2014).

[138] A. P. Miodownik, Calphad **1**, 133 (1977).

[139] G. V. Raynor and V. G. Rivlin, Bull. Alloy Phase Diagr. **2**, 102 (1981).

[140] S. V. Barabash, R. V. Chepulskii, V. Blum, and A. Zunger, Phys. Rev. B **80**, 220201(R) (2009).

[141] E. Lima and V. Drago, J. Magn. Magn. Mater. **280**, 251 (2004).

[142] R. W. Cochrane and G. M. Graham, Can. J. Phys. **48**, 264 (1970).

[143] I. Nakai, F. Ono, and O. Yamada, J. Phys. Soc. Jpn. **52**, 1791 (1983).

[144] A. Z. Menshikov, S. K. Sidorov, and V. E. Arkhipov, Zh. Eksp. Teor. Fiz. **61**, 311 (1971) [Sov. Phys. JETP **34**, 163 (1972)].

[145] M. Shiga, IEEE Trans. Magn. **8**, 666 (1972).

[146] A. Chamberod, J. Laugier, and J. M. Penisson, J. Magn. Magn. Mater. **10**, 139 (1979).

[147] M. J. Besnus, Y. Gottehrer, and G. Munschy, Phys. Stat. Sol. B **49**, 597 (1972).

[148] J. T. Lenkkeri, J. Phys. F: Met. Phys. **11**, 1991 (1981).